COMBUSTION OF PULVERIZED CHAR

C.R. McCann, J.J. Demeter, A.A. Orning, and D. Bienstock

U. S. Department of the Interior, Bureau of Mines,
Pittsburgh Energy Research Center, Pittsburgh, Pa.

Introduction

The increasing demand for natural gas stems from its freedom from emissions of particulate matter and sulfur oxides and its adaptability to relatively inexpensive and automatic combustion equipment. Many studies of fuel resources in the U.S. have indicated an impending shortage of natural gas. Fish[1] concludes that development of coal gasification is essential for the survival of the gas industry and indicates wellhead prices of natural gas will reach 50¢/MCF within 15 years.

Several coal gasification processes are being developed for production of pipeline gas. These generally yield a char residue that must be recovered for use as a solid fuel. The heating value in the char residue can amount to 50% of the heating value of the coal feed, depending on the process.

The combustion properties of chars are quite variable. A study based on the Coal Research Laboratory Reactivity Indices[2] shows a close correlation with the volatile matter content of cokes, reactivity decreasing with decreasing volatile matter content. The reactive properties of chars may differ, for material of the same volatile matter content, from those of cokes to those of active carbons. The reactivity of char residues from gasification will probably be nearer that for coke.

Walker[3] reported that chars from a fluidized bed process can be burned in pulverized form in furnaces normally used for anthracite or in conventional bituminous-type units with supplemental fuel. Craig and Smith[4] have burned the product of fluidized-bed coking of petroleum fractions in a slagging furnace without supplemental fuel. The furnace used opposed firing inclined downward to give flame impingement on the slag pool and very stable ignition.

Experience is limited, but indicates that char residues from gasification can be burned efficiently provided the furnace is designed for the particular fuel or an auxiliary fuel is used.

Tests such as those for the CRL Reactivity Indices or burning profiles, developed by Wagoner and Duzy[5] can be used to estimate relative ease of combustion, but may not be sufficient to predict combustion efficiency in a particular type of unit not designed primarily for handling low-volatile matter fuels. Also, the tests are not standardized nor are they generally available. This has resulted because data have not appeared that justify standardized reactivity tests in consideration of the close correlation between reactivity indices and the proximate analyses of solid fuels.

The present paper reports on the combustion experience with three chars of different volatile matter contents in a front-wall-fired, dry-bottom furnace capable of burning 500 lb of bituminous coal per hour.

Supplemental fuel was needed for stable combustion of low-volatile-matter chars in this unit. The proportion of supplemental fuel required, other operating variables held constant, is then a measure of the combustion properties of the given char. The percent carbon conversion in gasification should be optimized in relation to utilization of fuel value in the residual char, which in turn depends upon combustion properties of the char.

Experimental Apparatus

Combustion research has long been hampered by the unavailability of suitable equipment which could be used for experimental purposes. Present day industrial furnaces are too large, costly, and unwieldy to be used for experimentation, while results obtained from smaller experimental combustion units are difficult to interpret and extrapolate for use on full-scale furnaces. To overcome these liabilities, a multipurpose combustion unit was designed to simulate the performance of an industrial steam-generating furnace. The combustor, a dry bottom unit, is capable of burning 500 lbs of pulverized fuel per hour with an exit gas temperature of 2000°F. A photograph of the furnace is shown in Fig. 1. A simplified flowsheet of the combustion system including the pulverizing and feeding system is shown in Fig. 2. A cross-sectional view of the principal components, the combustor, convective heat transfer section, a duct designed for emission measurements, and a recuperative air heater is shown in Fig. 3. A detailed description of the furnace has been reported earlier.[6]

Operation

The four front-wall burners were designed to fire natural gas and/or pulverized solid fuel. Prior to each test period, the experimental furnace was fired with natural gas to preheat the refractory and to provide a source of preheat for the secondary air. During this period, combustion air flows were established and necessary secondary-air swirl adjustments were made to provide flames that were attached to the burners, but not drawn into the burner tubes. Preheating was then continued until the secondary air temperature reached about 550°F. Natural gas flow to each burner was then reduced by 50%, and pulverized-char feed was started at a rate of about 250 lbs per hour. From this point, oxygen content of the flue gas was used as a guide in the changeover. As the char feed rate was increased, natural gas to each burner was decreased to maintain a constant oxygen level in the flue gas. All of the chars fired in this investigation required supplemental fuel to provide stable flames. Since the burners are capable of burning pulverized solid fuels and natural gas, the latter was used as the supplemental fuel. Thus, the next operation was determination of the minimum amount of natural gas to provide stable flames.

When the desired char feed rate, nominally 400 lbs per hour, was reached, natural gas provided about 25% of the total thermal input to the furnace. Natural gas feed to each burner was then gradually decreased to the minimum amount necessary to produce stable flames, as determined by observation of the burners. Final adjustments were then made on char feed rate and secondary air to provide the desired excess air level for the test period.

Char used in this investigation was produced in an entrained carbonizer using Utah King HVBA as the parent coal. About 50 tons of coal were processed in 3 batches, each batch yielding a different volatile-level char, nominally 5, 12, and 15 percent by weight. During each combustion test, a char sample was taken from the primary air-fuel stream using a small cyclone sampler, the tip of which extended into the center of the recirculation loop. A typical analysis of char of each volatile level and of the parent coal is given in Table I.

TABLE I.- Typical analyses of chars and parent coal

	Low volatile char	Medium volatile char	High volatile char	Utah King mine coal
Proximate, wt-pct, as received				
Moisture	0.8	2.8	2.6	4.9
Volatile matter	5.1	12.0	15.1	44.0
Fixed carbon	80.9	73.2	72.0	45.9
Ash	13.2	12.0	10.3	5.2
Ultimate, wt-pct, as received				
Carbon	81.6	75.9	75.5	72.3
Hydrogen	1.0	2.3	3.0	5.8
Nitrogen	1.4	1.7	1.8	1.3
Sulfur	0.5	0.6	0.6	0.5
Oxygen	2.3	7.5	8.8	14.9
Ash	13.2	12.0	10.3	5.2

Discussion of Results

Supplemental fuel requirements varied for each volatile level and, to a lesser degree, for each set of combustion conditions within a volatile level. Minimum fuel requirements, determined as percent of total enthalpy input are shown graphicly in Fig. 4. The plot shows that minimum supplemental fuel depends somewhat upon the amount of preheat in combustion air. Extrapolation of the curves indicates that volatile matter content in excess of 20% is required for combustion of this char without supplemental fuel addition.

Combustion tests were performed according to a factorially designed program using three independent variables, each at two levels, as follows:

Variables*	Levels
Excess air	5 and 20%
Secondary air preheat	600° and 700°F
Degree of pulverization	80 and 95% thru 200 mesh

*Supplemental fuel, as percent of total heat input, was also a variable, but as indicated above, it was not an independent variable.

When minimum auxiliary fuel requirements were met, chars of each volatile level burned with very stable flames. Table II is a summary of the experimental data from the combustion tests. Carbon combustion efficiencies greater than 99% were obtained with char containing 15% volatile matter. Even with the more undesirable combustion variables--low air preheat, low excess air, and large fuel particle size, the low volatile char yielded about 94% carbon combustion efficiency.

Figure 5 shows the effect of volatile matter content on carbon combustion efficiency, with excess air and fuel particle size as combustion parameters. While the experiments were factorially designed for each volatile level of char individually, the data were subjected to regression analysis, since this type of analysis permitted addition or transformation of variables, and analyses of all of the data as a single block. The analyses yielded an equation as follows:

TABLE II.- Summary of experimental data

Observation No.	Excess air, pct	Degree of pulverization, pct, thru 200 mesh	Air preheat temp., °F	Volatile matter content percent, as fired	Carbon combustion efficiency, pct	Percent of total heat input in natural gas
31	19.6	95.2	700	5.2	97.5	15.4
32	5.4	95.2	695	5.2	95.5	15.0
33	10.6	94.9	600	4.7	97.2	14.6
34	5.4	94.9	600	4.7	95.2	15.2
35	19.0	80.1	605	5.0	95.3	15.2
36	4.9	80.1	600	5.0	93.8	14.8
37	19.6	80.3	690	5.6	95.7	15.2
38	4.9	80.3	695	5.6	94.0	14.7
91	19.6	95.1	700	12.5	98.7	12.0
92	4.9	95.1	695	12.5	97.5	11.9
93	20.2	95.0	605	11.9	98.3	13.0
94	5.0	95.0	600	11.9	97.2	13.2
95	20.3	79.8	600	12.1	97.3	13.9
96	4.9	79.8	600	12.1	95.7	13.8
97	20.3	80.2	690	11.5	97.5	11.8
98	4.9	80.2	690	11.5	96.0	12.3
151	19.6	95.0	700	15.3	99.8	8.9
152	5.4	95.0	700	15.3	99.5	9.6
153	18.2	94.9	600	16.0	99.5	10.9
154	4.9	94.9	600	16.0	99.2	10.4
155	18.9	79.9	600	14.9	99.1	10.8
156	4.9	79.9	600	14.9	98.1	11.0
157	19.6	80.0	705	14.9	99.4	9.2
158	4.9	80.0	695	14.9	98.5	9.5

$$\text{Carbon combustion efficiency} = 85.5 + .077A + .067B + .00347C + 1.3 \times 10^{-6} D^2 + .0007E$$

where A = excess air, percent
B = degree of pulverization, percent thru 200 mesh
C = heating value of volatile in char, Btu/lb char as fired
D = (C - 1400)
E = thermal input in preheated air, Btu/lb char.

Heating value of volatile in the char, C, was calculated by difference in the heating value of the char and the heating value of the fixed carbon in the char, assuming 14,500 Btu/lb of fixed carbon.

Of interest in the equation is the absence of a term showing the effect of the natural gas used to provide flame stabilization. As the volatile matter content of the char was decreased, it was necessary to increase the percent of total heat input supplied by natural gas in order to maintain a stable flame. The percent of heat input supplied by natural gas was not an independent variable. Accordingly, the effect of natural gas is included in the effect of the heating value in the volatile of the char.

Analyses of the data indicate that excess air, degree of pulverization, heating value of the volatile in the char, and the quadratic effect of the heating value of the volatile in the char are about equally important, while air-preheat temperature is of marginal significance. Over 95% of the variation in carbon combustion efficiency is explained by the equation.

Conclusions

The combustor used in this investigation simulated the operation of a dry-bottom, horizontally-fired, pulverized-coal furnace. When fired in this unit, chars with about 5% volatile matter yielded 94-97.5% carbon combustion efficiency, while 12% volatile char yielded 95.7-98.7%, and 15% volatile char yielded 98.1-99.8% carbon combustion efficiency. The ranges of carbon combustion efficiency were the effect of the combustion parameters--excess air, fuel particle size, and secondary air preheat. As expected, higher excess air and higher preheat with fine particle size yielded higher efficiencies. All of the chars fired required supplemental fuel to provide flame stabilization. The amount required, based on percent of total enthalpy input, was about 10, 13, and 15% natural gas for chars containing 15, 12, and 5% volatile matter, respectively. It appears that a volatile matter content in excess of 20% is necessary for combustion of these chars without supplemental fuel.

References

1/ Fish, L.W., Am. Gas Assoc. Monthly 53, 8-9 (March 1971).
2/ Orning, A.A., Ind. Eng. Chem. 36, 813-16 (1944).
3/ Walker, J.B., Jr., Steam from By-Product Fuels, Paper presented at A.S.M.E. Annual Meeting, New York, N.Y., Dec. 1-6, 1957, (57-A-126).
4/ Craig, O., and Smith, E.H., Mech. Engr. 78, 921-25 (1956).
5/ Wagoner, C.L., and Duzy, A.F., Burning Profiles for Solid Fuels, Paper presented at A.S.M.E. Winter Annual Meeting and Energy Systems Exposition, Pittsburgh, Pa. Nov. 12-17, 1967, (67-WA/FU-4).
6/ McCann, C.R., Demeter, J.J., Orning, A.A., and Bienstock, D., NO_x Emissions at Low Excess-Air Levels in Pulverized-Coal Combustion, Presented at the A.S.M.E. Winter Annual Meeting, New York, N.Y., Nov. 29-Dec. 3, 1970, (70-WA/APC-3).

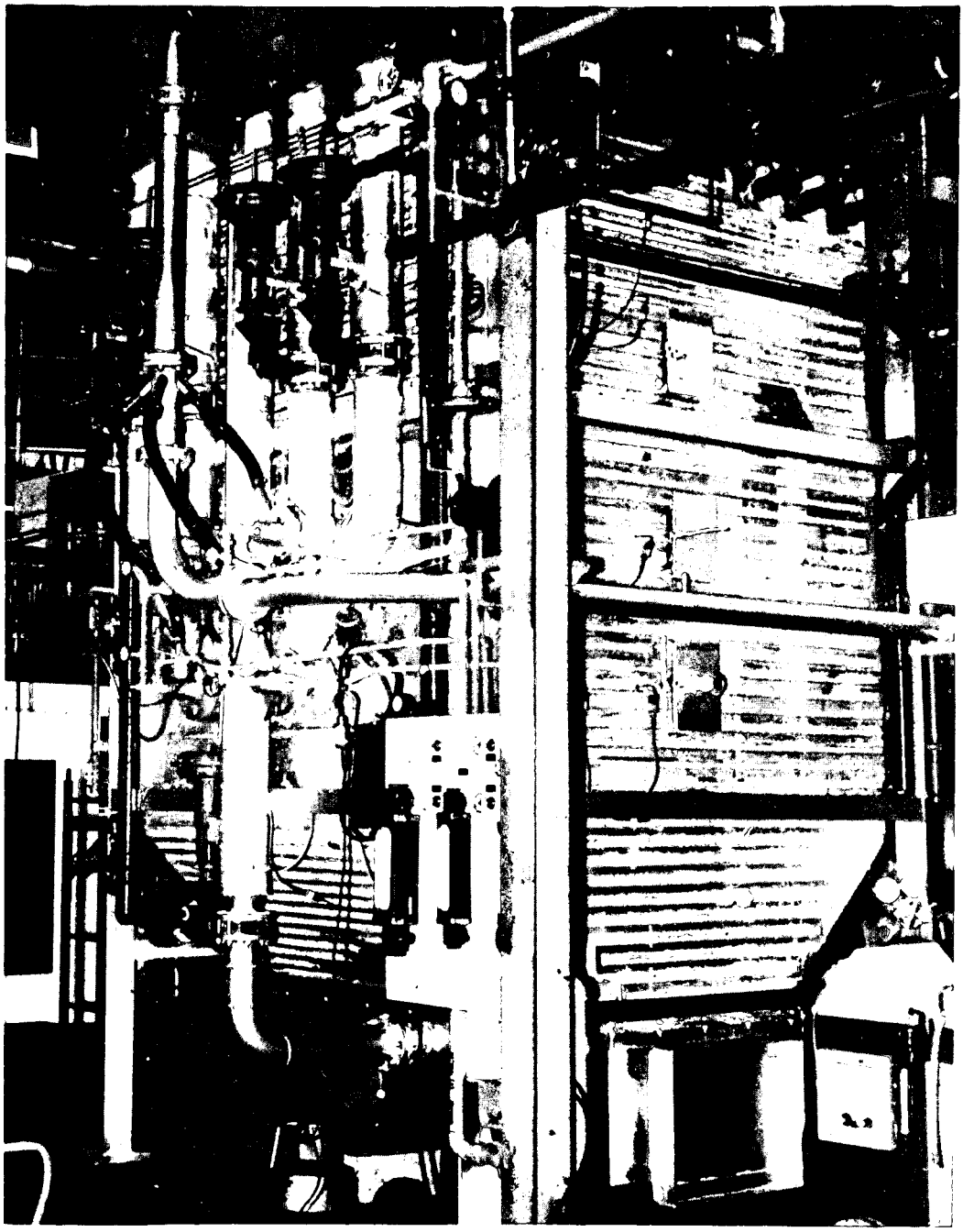

Figure 1.- Pulverized-Coal-Fired Combustor.

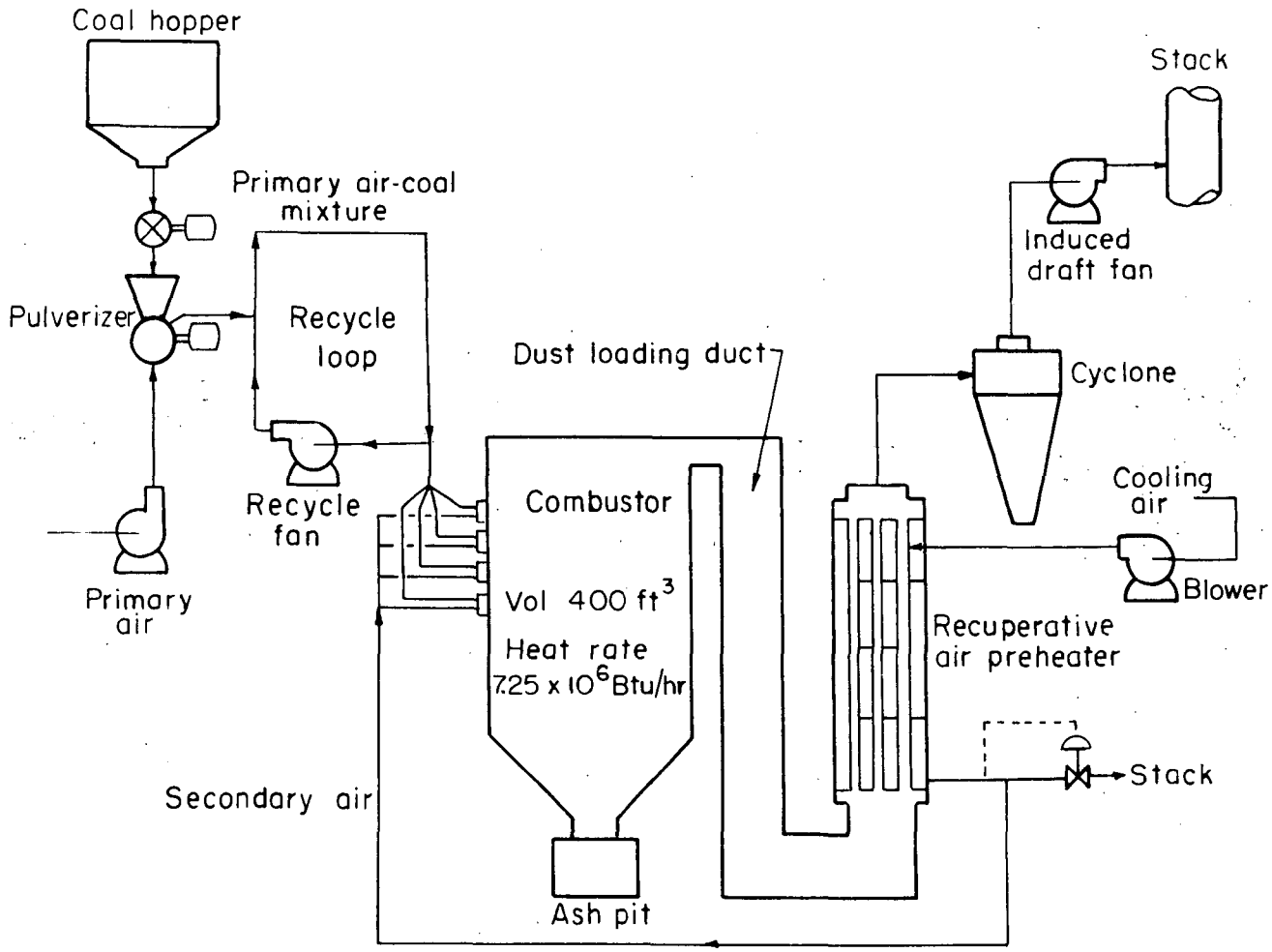

Figure 2—Simplified flowsheet of 500 lb/hr pulverized-fuel-fired furnace.

L-11323

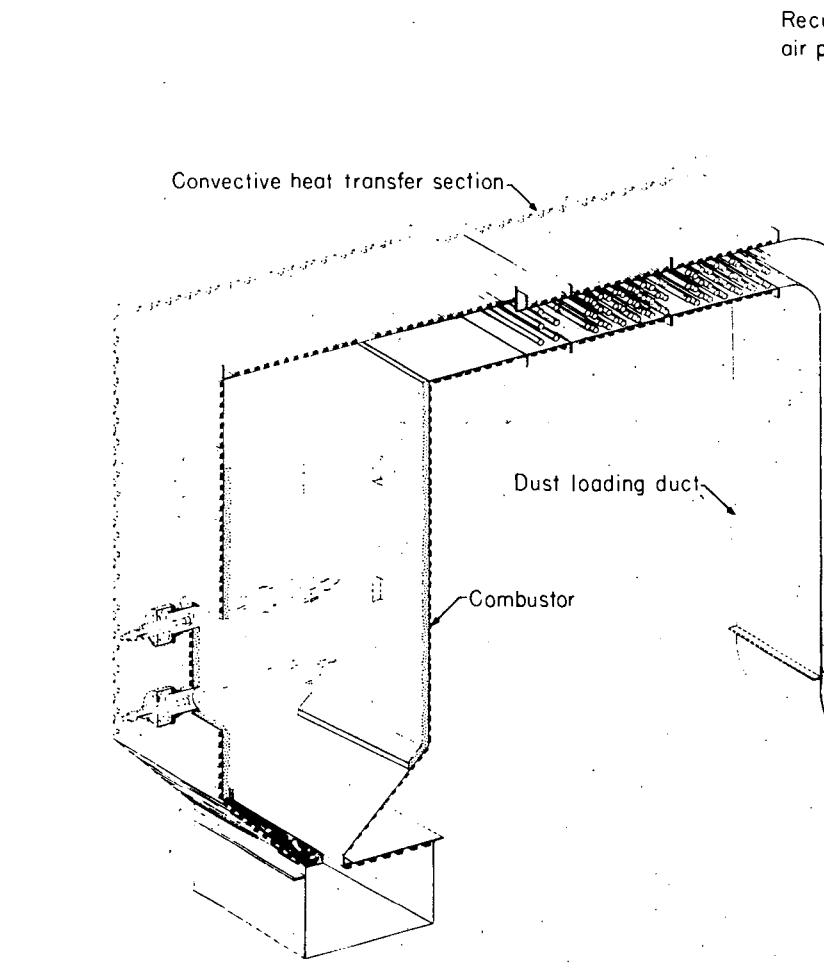

Figure 3.- Cross-sectional view of 500 lb/hr pulverized-fuel coal combustor.

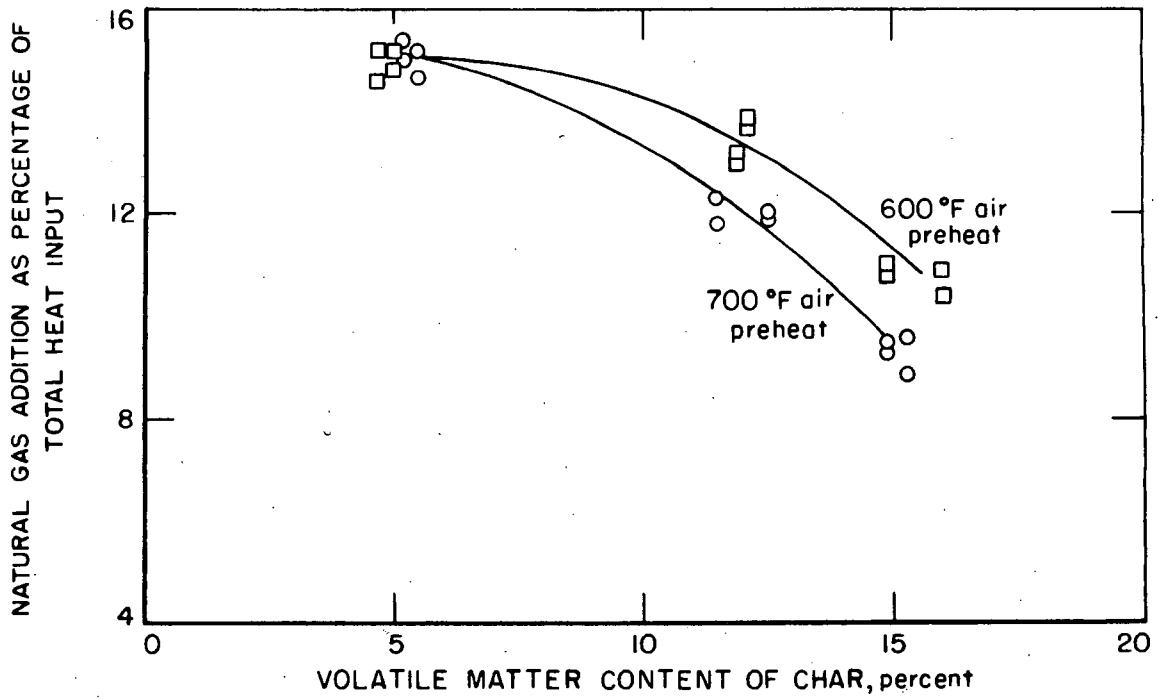

Figure 4—Supplemental fuel requirement as a function of volatile matter content.

L-12249

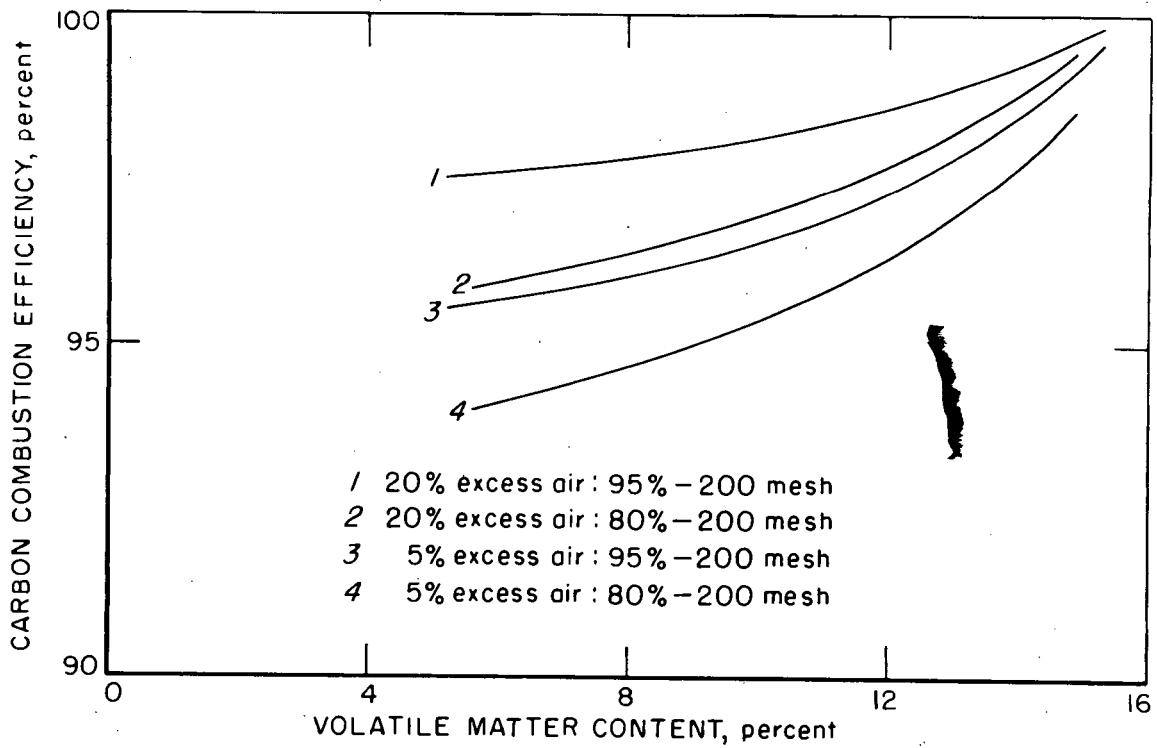

Figure 5– Carbon combustion efficiency as a function of excess air with 700° F preheat.[1]

[1]Sufficient natural gas added to stabilize combustion (See figure 4)

L-12248

DETECTION OF METHANE COMBUSTION WITH APPLICATIONS TO QUENCHING COAL MINE EXPLOSIONS

By J. E. Nealy* and W. L. Grose**

NASA Langley Research Center, Hampton, Virginia

ABSTRACT

A device developed by the U.S. Bureau of Mines for the detection and quenching of coal mine explosions suffers from the inability to discriminate between the light emitted from hydrocarbon combustion and that emitted by electrical sparks and miner's cap lamps. Since the quenchant device is activated by an internal explosive charge, the possibility of serious injury to nearby personnel demands a detector which can reject false signals. Described herein is a device which can provide a rapid response signal upon the emission of radiation from hydrocarbon combustion and concurrently reject spurious signals from such sources as sparks and cap lamps.

NOMENCLATURE

B_λ	Planck blackbody function - watts/cm^2-μ
I	intensity - watts/cm^2
$j_{\Delta\lambda}$	spectral emission coefficient for bandpass $\Delta\lambda$ - watts/particle
n_{OH}	number density of OH particles - particles/cm^3
V	volume - cm^3
μ_λ	absorption coefficient - cm^{-1} particle^{-1}
ω	solid angle - steradians

*Aerospace Engineer, Hypervelocity Impulse Facilities Section, Hypersonic Vehicles Division.

**Aerospace Engineer, Flow Field Kinetics Section, Hypersonic Vehicles Division.

INTRODUCTION

The accumulation of methane gas in a coal mine constitutes an ever present explosion hazard. The methane is a by-product of the decomposition process which forms the coal. If the concentration of methane in air reaches the critical range of approximately 5-12 percent an explosion can occur. Methane levels are customarily controlled by forced ventilation, but this is not completely successful in preventing localized concentrations in the critical range.

An explosion takes a finite time period (on the order of milliseconds) to develop after ignition of the methane. The U.S. Bureau of Mines has developed a device for detecting and quenching the developing explosion by discharging potassium bicarbonate in its path (refs. 1 and 2). However, the device is unable to discriminate between light emitted from methane combustion and that emitted by electrical sparks or miner's cap lamps. Since the quenchant device is dispersed by an internal explosive charge, the possibility of serious injury to nearby personnel demands a detector which can reject false signals. It was suggested by R. L. Trimpi, Assistant Chief, Hypersonic Vehicles Division, Langley Research Center, that this difficulty might be surmounted by developing a detector which would operate on the principle of monitoring the radiation intensity emitted from two separate spectral regions and ratioing the intensities . Such a detector would provide a rapid response signal after sensing the emission of radiation from the hydrocarbon combustion and concurrently reject spurious signals from sparks and cap lamps due to the differences in the spectral characteristics of the emissions.

A series of experiments are described for methane-air combustion which illustrate the validity of such an approach. Estimates of the spectral irradiance of the combustion event are presented, thereby determining the required sensitivity of the device.

EXPERIMENTAL APPARATUS

A cylindrical (3.8" diameter x 12") stainless steel shock tube test section was used as a combustion chamber. The test section was equipped with quartz windows (2" diameter) on either side, a piezoelectric pressure transducer, and two steel electrodes. A 10 kilovolt capacitor discharged across the electrodes provided a sub-microsecond duration spark to ignite the gas mixture within.

The desired partial pressures of methane and air were obtained by using a Wallace and Tiernan 0-800 mm Hg pressure gauge with which pressures could be determined to an accuracy of 1/2 mm Hg. All tests were conducted with a total pressure of 1 atmosphere in the chamber. The time history of the wall pressure was measured during combustion with a Kistler Model 701 Quartz Pressure Transducer and Charge Amplifier.

The radiation emitted during combustion was observed with Jarrell Ashe 1/4 meter monochromators placed symmetrically on either side of the test section. The monochromator dispersion was 33 Å/mm and both entrance and exit slits were 500 μ in width. Radiation emerging from the exit slits was detected with RCA 1P28 photomultiplier tubes. A Philbrick Model Q3M1P operational amplifier was used to ratio the output voltage from the two spectral channels. All signal voltages were recorded on Tektronix Models 551 and 556 oscilloscopes.

A schematic diagram of the experimental apparatus is shown in figure 1.

RESULTS

A survey of the flame spectrum of methane showed that a particularly strong emission occurred from the OH 0-0 band head at 3064 Å, and that a region of relatively low emission existed nearby at 3000 Å. Several ignitions were performed with the monochromators set on these channels to check consistency, and in all cases were found to repeat well, with an approximate intensity ratio of 6:1, and a peak wall pressure of 75 psia. An oscilloscope trace made during one of these tests in a stoichiometric mixture of methane and air is shown in figure 2.

Next, a series of ignitions was carried out in which the initial partial pressure of methane was varied through the combustion range of 5-12 percent. In these tests, it was found that the 6:1 intensity ratio was approximately maintained, even though the relative intensities varied considerably with initial CH_4 concentration. A plot of relative peak intensity for both channels as a function of initial partial pressure of methane is shown in figure 3, along with the peak wall pressure variation.

Figures 4 and 5 illustrate the electronic ratio of the signals of the two spectral channels. The records of figure 4 were made with the monochromators at the normal test configuration 6 inches from the test section centerline, while those of figure 5 correspond to a position 18 inches from the centerline. It is seen that even though the relative intensities have been greatly reduced, use of the operational amplifier to divide the incoming phototube signals minimizes the variation of output signal as a function of source detector distance.

For light sources emitting radiation in both channels, such as the incandescent lamp continuum on the many-line spectrum of iron, the signal ratio should be significantly reduced. Figure 6 shows the individual channel outputs for a 200 watt tungsten lamp and the corresponding ratioed signal from the operational amplifier. Similar results are obtained for an iron arc source, as shown in figure 7.

The components used in the "bread-board" experiment immediately suggest the use of more compact and less expensive spectral ratioing devices as a hydrocarbon combustion detector. For example, narrow band interference filters placed in front of solid-state photodetectors equipped with an electronic divider circuit could be operated from a central power supply or optionally from a self-contained battery pack. Electronic dividers are commercially available in wafer size integrated circuits, as are 25 Å bandpass filters in this wavelength region.

In order to assess the sensitivity requirements of such a prototype, the intensity, I, received at the detector may be approximated by the following:

$$I \simeq \frac{n_{OH}\ \omega\ V}{4\pi} \int_{\Delta\lambda} \mu_\lambda\ B_\lambda\ d\lambda \equiv \frac{n_{OH}\ \omega\ V}{4\pi}\ j_{\Delta\lambda}$$

where $j_{\Delta\lambda}$ is the integral over the specified bandpass (.3064 - .3089 μ) of the emission coefficient of an OH particle and is a function of temperature only. This function has been calculated from the absorption coefficient tabulations of reference 3 and is presented in figure 8.

This information, along with the number density of OH particles in burning volume V at temperature T, and the solid angle, ω, subtended

by the detector, may be used to approximately determine the sensitivity requirement of a photodetector. Reference 4 gives typical mole fractions of OH as .02 at flame temperature 1960° K for a methane-air mixture at 1 atm. pressure. Choosing a representative volume of 28400 cm^3 (1 ft^3) and solid angle of 10^{-5},

$$I \simeq \frac{1}{4\pi} [7.5(10)^{16} \cdot 10^{-5} \cdot 2.84(10)^{4} \cdot 10^{-23}] \simeq 10^{-8}$$

The RCA 1P28 photomultipliers used have a photosensitivity rating of about 50 ma/watt at .3μ and a current gain of 2 $(10)^5$. This results in a cathode current of .1 ma, which through a 10 K output resistor supplies 1 volt signal to the divider, which is more than adequate.

CONCLUSIONS

It has been demonstrated that methane combustion produces much greater emission near .3064 μ than at .3000 μ, whereas electric sparks and incandescent lamps possess nearly constant emission levels in these spectral regions. Therefore, a detection scheme based on the ratio of the emission at these wavelengths can discriminate between methane combustion and the interjection of an incandescent lamp or an electric spark in the optical field of view. Estimates of the spectral irradiance of methane combustion have been made and indicate adequate detector sensitivity for representative conditions.

Although these experiments were conducted for CH_4 combustion, the detection apparatus should respond similarly for other hydrocarbon combustion processes due to formation of the OH radical.

REFERENCES

1. Mitchell, D. W.; Nagy, J.; Murphy, E. M.: Preventing Explosions from Gas Ignition at the Face. Bureau of Mines Report, Sept. 1967.

2. Kamenski, E. M.; Nagy, J.; Conn, J. W.: Further Development of an Explosion Quenching Device. International Conference of Safety in Mines Research, Tokyo, Japan, Nov. 1969.

3. Golden, S. A.: Spectral Absorption Coefficients of Electronic Transitions in Diatomic Molecules. Vol. 2, Part C, ARPA Report.

4. Gaydon, A. G.; and Woldhard, H. G.: Flames - Their Structure, Radiation and Temperature. Chapman and Hall, Ltd., 1960.

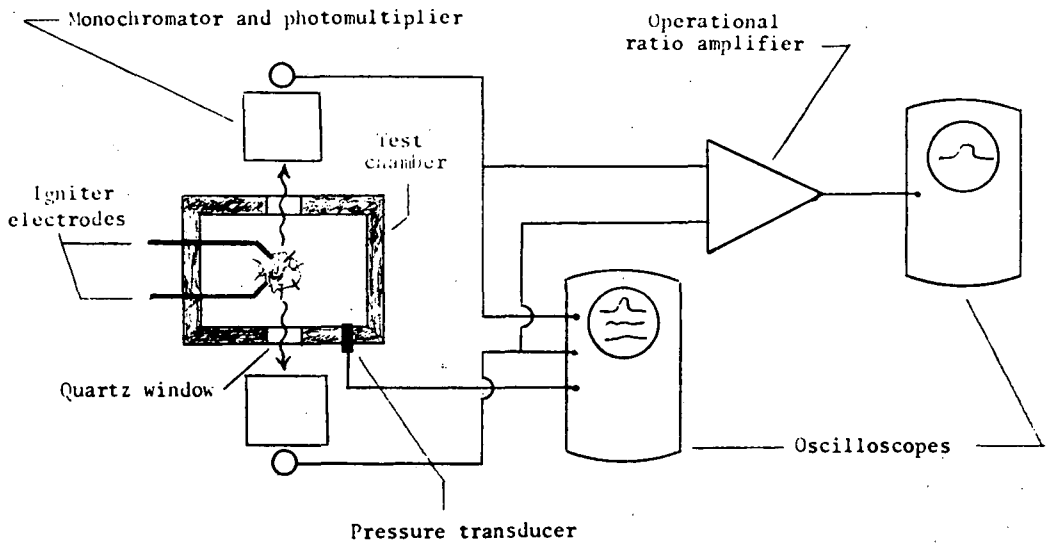

Fig. 1. Schematic diagram of experimental apparatus.

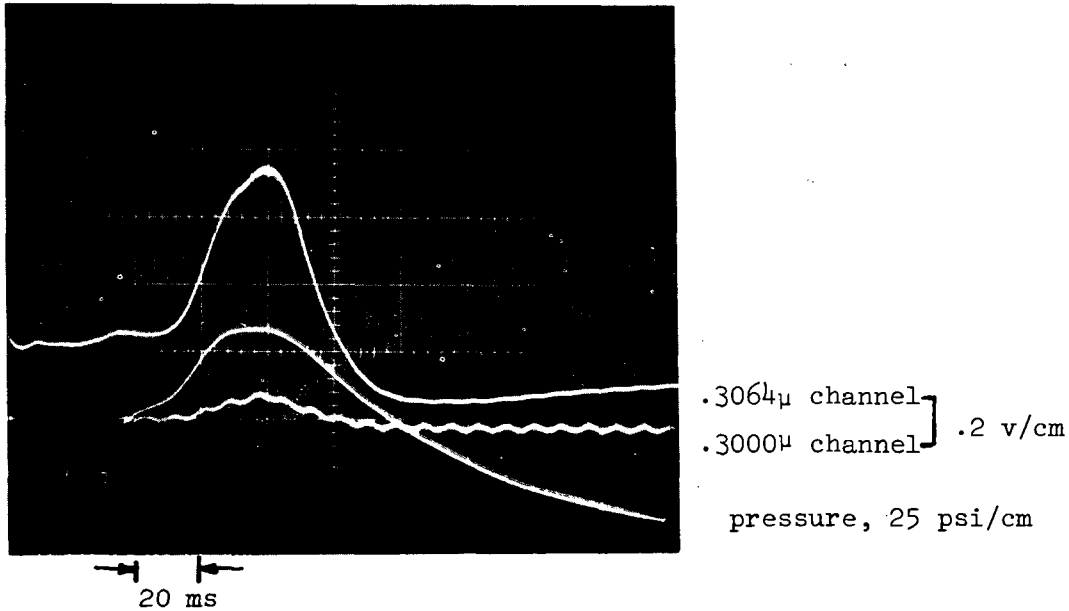

Fig. 2. Photomultiplier outputs and pressure transducer signal for typical combustion.

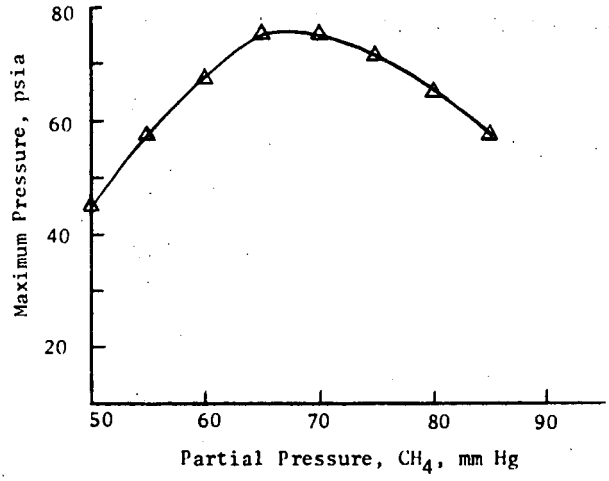

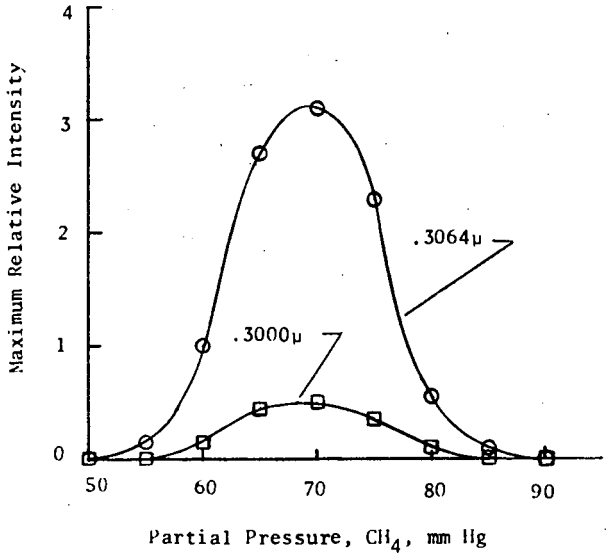

Fig. 3. Plots of peak spectral intensities and maximum pressures as functions of initial partial pressure of CH_4 in air.

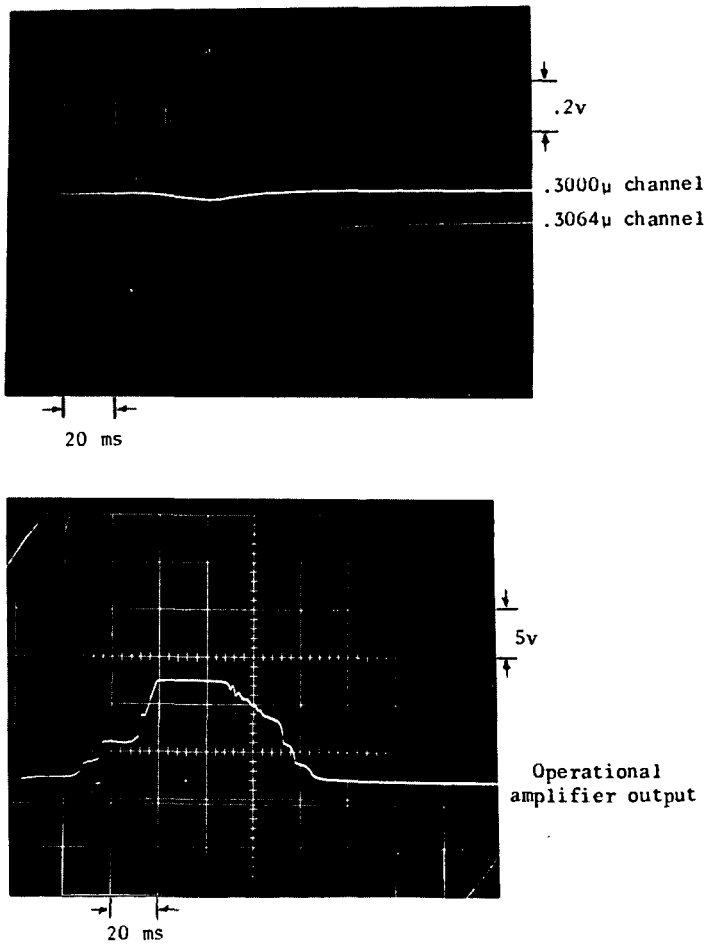

Fig. 4. Record of spectral intensities and output of electronic ratio amplifier during typical combustion test.

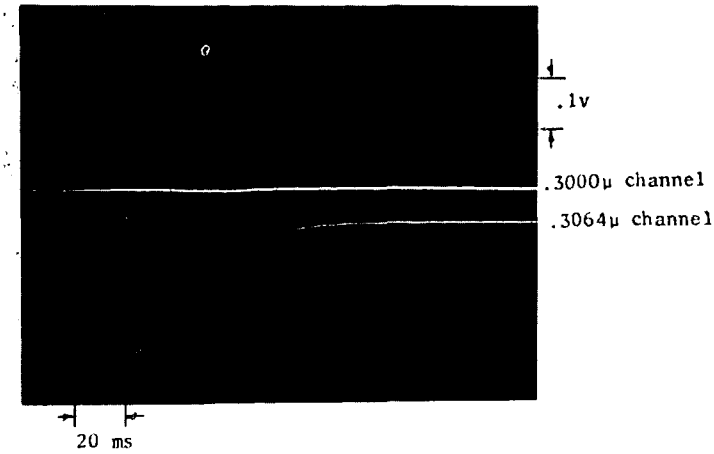

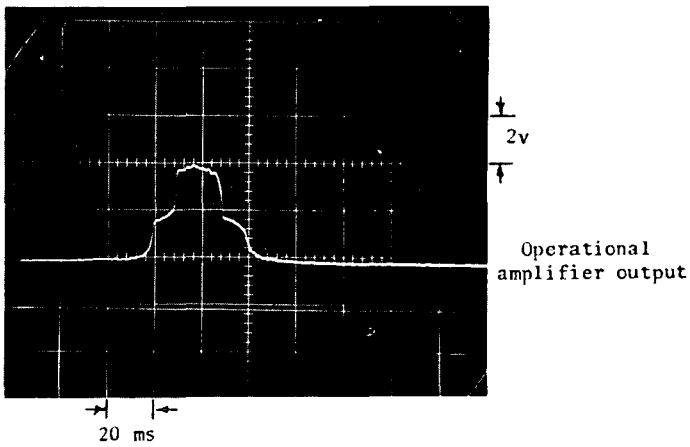

Fig. 5. Record of spectral intensities and output of ratio amplifier with reduced intensity on spectral channels.

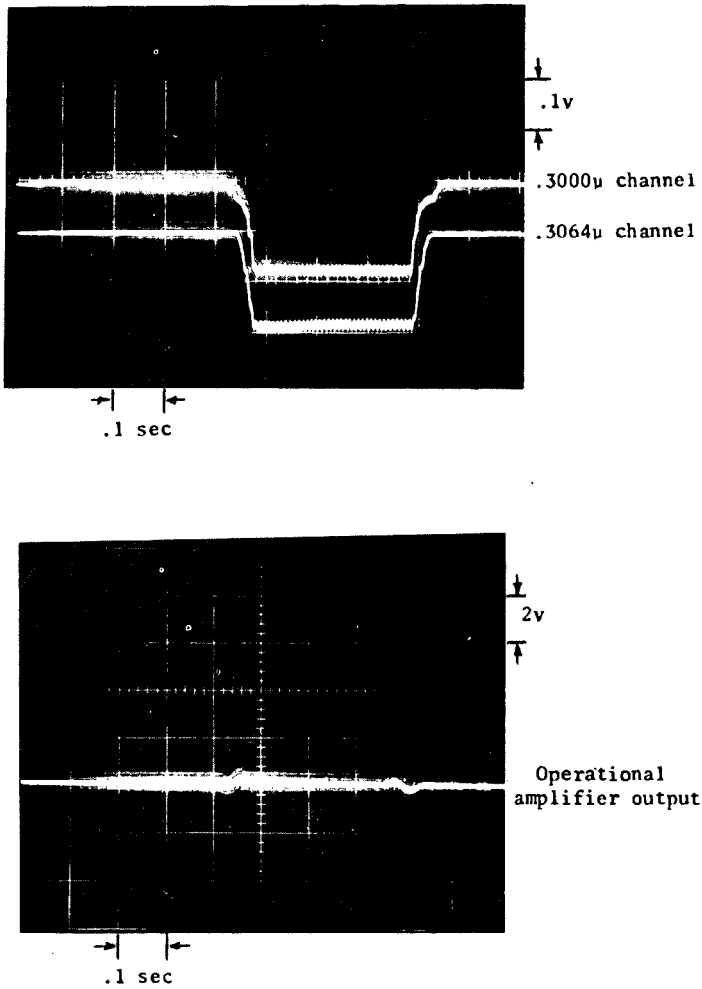

Fig. 6. Spectral signals and output of ratio amplifier for incandescent lamp.

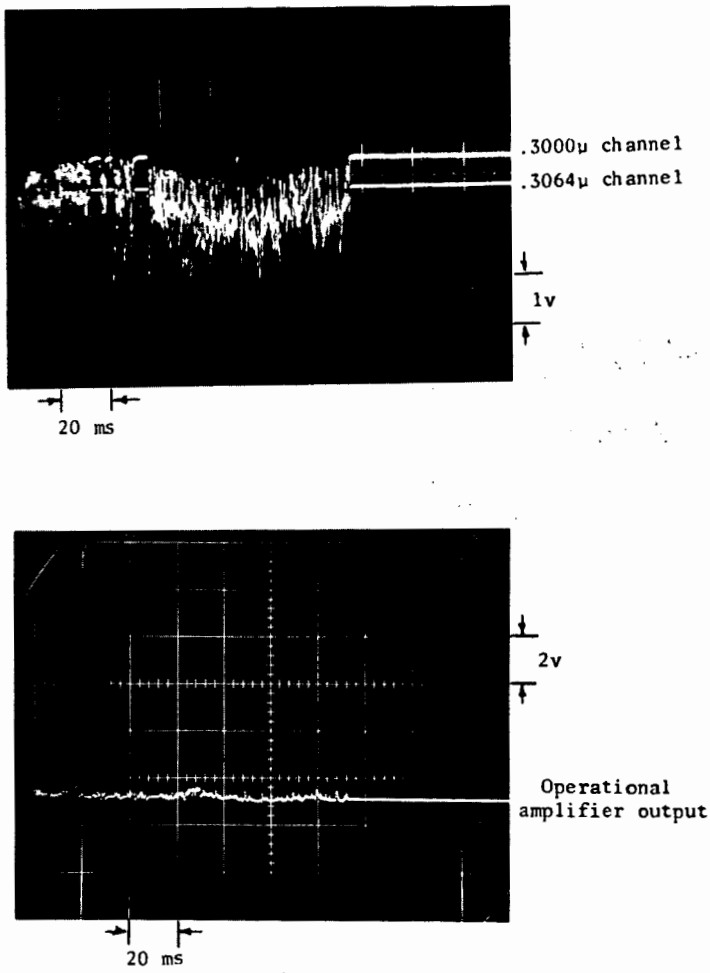

Fig. 7. Spectral signals and ratio amplifier output for iron arc source.

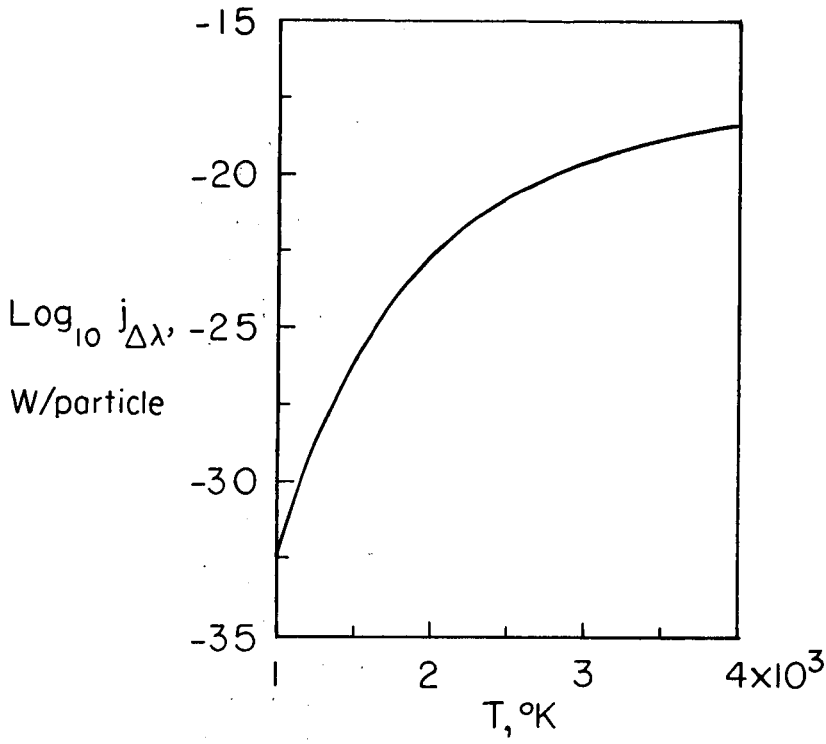

Fig. 8. Spectral bandpass energy per OH particle as a function of temperature.

ANALYTICAL RELATIONSHIPS FOR THE INFLUENCE OF PARTICLE SIZE ON PRECIPITATOR DESIGN

by

Robert G. Kunz and Owen T. Hanna

Introduction

The realistic design of many types of particulate collection devices involves consideration of the influence of particle size distribution. For an electrostatic precipitator, this influence is appropriately expressed by the integration of the Deutsch equation for a log-normal particle size distribution. The integral which must be evaluated in such cases depends on several parameters and cannot be evaluated exactly in terms of elementary functions. A numerical tabulation of the integral for all parametric cases of interest, while feasible, poses a considerable numerical interpolation problem and is not very suitable for computerization.

In order to express the integral simply and accurately, asymptotic methods are employed in this paper. These methods produce analytical approximations which are expressed in terms of well known functions and the solution of a certain nonlinear algebraic equation. Results of these calculations are given here in forms suitable for either hand or computer calculations. Comparison with numerical calculations shows that the results of the asymptotic analysis are applicable for virtually all cases of practical interest.

Electrostatic Precipitator Theory

In an electrostatic precipitator, suspended dust particles in a gas are electrically charged and migrate to collecting surfaces where they are captured. A force balance on a single charged particle in a quiescent gas under the influence of an electric field produces the following expression for the particle migration velocity:

$$w = \frac{E_o E_p d_p}{4\pi\mu} \tag{1}$$

The collection efficiency of a precipitator in turbulent flow is then given by the Deutsch equation

$$\eta = 1 - e^{-A_p w/Q} \tag{2}$$

However, the value of w calculated according to first principles from eqn. (1) with its underlying simplifying assumptions may be several times too high because of effects unaccounted for in its derivation. These include multiple particles, uneven gas distribution, particle reentrainment, and high dust resistivity, as comprehensively discussed by White.[11, 12] Therefore, to predict the operation of an actual precipitator, the theoretical migration velocity is replaced by a precipitation rate constant based on experience.[6]

Log-Normal Particle Size Distribution

Moreover, the particles encountered in practice are not uniform in size as we have so far tacitly assumed, but rather are made up of a continuous distribution of sizes. Specifically, most powders of industrial significance are log-normally distributed. The frequency of occurrence of a given diameter particle plotted against the logarithm of that size produces the familiar bell-shaped curve. Alternatively, the logarithm of the particle diameter (d_p) graphs as a straight line against cumulative weight percent less than that size. An example of the latter plot is shown in Figure 1. Two parameters, the mass median diameter ($\bar{d}_p$) and the geometric standard deviation (σ) completely specify the distribution. The mass median diameter is the diameter at the 50% point, and σ is given by either of the following ratios:

$$\bar{d}_p/d_p \text{ at } 15.9\% \text{ or } d_p \text{ at } 84.1\%/\bar{d}_p$$

A more complete explanation of fine particle statistics is contained elsewhere.[5]

Collection Efficiency Log-Normal Distribution

By lumping all non-size related quantities into one parameter

$$k = \frac{E_o E_p A_p}{4\pi\mu Q} \tag{3}$$

eqn. (2) can be written

$$\eta = 1-e^{-kd_p} \tag{4}$$

Eqn. (4) is exponential in character although k, like w, is empirical. This function, shown in Fig. 2, is an example of the so-called grade efficiency curve discussed by Stairmand.[8-10] Typically, larger particles are collected much more readily than smaller ones.

With the grade-efficiency function defined, the collection efficiency for each individual particle size in the distribution is completely determined. The overall efficiency of collection (η) is obtained by summing up these individual contributions

$$\eta = 1 - \frac{1}{\sqrt{2\pi}} \int_{-\infty}^{+\infty} e^{-\frac{t^2}{2} - ae^{bt}} dt \tag{5}$$

where $a \equiv k\bar{d}_p$ and $b \equiv \ln \sigma$

Although attention has been focused on electrostatic precipitators, the technique to be outlined below applies as well to other types of particulate collection devices whose grade-efficiency curves can be approximated

by eqn. (4). Typical grade-efficiencies replotted on semi-logarithmic coordinates from Stairmand's tabulations and curves are shown in Fig. 3 for several such devices. Increasingly efficient collection is reflected by a larger value of k.

Numerical Integration

The integral of eqn. (5) can be computed directly by numerical quadrature, resulting in the curves presented in Fig. 4. For some purposes, these curves will be entirely satisfactory. More than likely, however, collection efficiency will be desired for a set of input parameters a and b not corresponding exactly to any of these curves, requiring either an interpolation or a complete numerical re-evaluation of the integral. In other words, the functional dependence of the efficiency on the input parameters is not shown explicitly. For this reason, simple and accurate analytical approximations for this integral have been developed.

Approximate Representation of $\frac{1}{\sqrt{2\pi}} \int_{-\infty}^{\infty} e^{\frac{-t^2}{2} - ae^{bt}} dt \equiv I$

This infinite integral is seen to converge for all values of a and b. The integrand $\to 0$ for both $t \to -\infty$ and $t \to \infty$ and thus, since the integrand is always positive, it must have a maximum value at some point t^*. At the maximum point t^*, the usual condition for an interior maximum requires that

$$t^* + abe^{bt^*} = 0 \tag{6}$$

It is easily verified that there can be but one maximum point t^* for any given set of values of a and b. Thus t^* depends on both a and b. However, by changing the variables to $t^* \equiv a^{1/2} u^*$ and $C \equiv a^{1/2} b$, eqn. (6) is reduced to a form involving the single parameter C as follows:

$$u^* + Ce^{Cu^*} = 0 \tag{7}$$

Since the integrand involves exponentials, it is natural to hope that by investigating the maximum of the integrand and suitably changing variables, the original integral might be transformed to one of the Laplace type, which could then be evaluated approximately for certain limiting values of a or b.[2] However, in this problem a transformation of this type does not yield the desired Laplace integral, but the transformation is nevertheless extremely useful since it does lead ultimately to a resolution of the original problem.

Some details of the analysis involved in approximating the integral are given in the appendix for the reader who is interested. Here we will present the essential results of the analysis. First we note that the approximation formulas depend on the solution of nonlinear eqn. (7). The solution of this equation is indicated graphically in Fig. 5. Approximate analytical solutions of this equation accurate to better than 5% are developed in Appendix I. These approximations may be used directly, or, if more accuracy is desired, they may be used as first guesses for iteration schemes that are also outlined in this appendix. This approach is very attractive for use on the digital computer.

The most useful approximation of the original integral I is as follows:

$$I \doteq \frac{e^{\frac{-A^2b^2}{2}} - A}{(1+Ab^2)^{1/2}} \quad (a \to \infty,\ a \to 0,\ b \to 0) \tag{8}$$

The quantity A in eqn. (8) is related to the solution of nonlinear eqn. (7) since $Ab^2 \equiv -Cu^*$ and the solution of eqn. (7) is expressed in terms of this quantity.

Eqn. (8) is a simple expression which approximates the original integral very well, as shown in Table 1. In Appendix II, it is proved that eqn. (8) is valid in the limit of either $a \to \infty$, $a \to 0$, or $b \to 0$. The fact that eqn. (8) applies for so many limiting cases gives some reason for its excellent agreement with numerical results over such a wide range of a and b values. Except for the impractical case of large b(log-normal probability particle size distribution approaching a vertical line), the approximation would produce results coincident with the curves of Fig. 4.

Eqn. (8) represents the first approximation of an asymptotic expansion for the limiting cases quoted, and it is generally possible to increase the accuracy of the approximation by adding in some correction terms. However, adding only the next uniformly valid contribution for $a \to 0$, $a \to \infty$, $b \to 0$ causes the formula to become very much more complicated. Moreover, the comparison between eqn. (8) and the numerical results shown in Table 1 indicates that correction terms are not really necessary.

Although eqn. (8) seems to represent an appropriate approximation to the original integral I for current needs, it is difficult to anticipate whether some cases that seem unimportant now will prove to be significant at a later time. For this reason and for the sake of completeness, certain other approximations to I are given in Appendix III.

Approximate Representation of $\frac{1}{\sqrt{2\pi}} \int_{-\infty}^{z} e^{\frac{-t^2}{2} - ae^{bt}} dt \equiv J$

Frequently an estimate of the particle size distribution of the uncollected material is required in addition to an overall efficiency prediction. This would be important where several collecting devices are to be installed in series. For example, it is not uncommon for cyclones to be installed upstream of a precipitator. In this case, the quantity and distribution of the particulates escaping from the cyclones would be used as the feed to the precipitator, and the calculation repeated.

To calculate the particle size distribution, it is desirable to approximate the above integral where $z = \ln(dp/\overline{dp})/b$ is now a parameter in addition to a and b. It appears possible to do this in a manner analogous to that for the previous case ($z \to \infty$). Again, the details are indicated in the appendix (Appendix IV). The result is

$$(z<t^*) \qquad J \doteq \frac{e^{\frac{-z^2}{2} - E + \frac{(z+Eb)^2}{2(1+b^2E)}}}{\pi^{1/2}(1+b^2E)^{1/2}} \int_{s = -\frac{z+bE}{2^{1/2}(1+b^2E)^{1/2}}}^{\infty} e^{-s^2} ds \qquad (9)$$

where $E \equiv a\, e^{+bz}$.

Eqn. (9) holds only for $z<t^*$. For $z>t^*$, we have instead

$$(z>t^*) \qquad J \doteq I - \frac{e^{\frac{-z^2}{2} - E + \frac{(z+bE)^2}{2(1+b^2E)}}}{\pi^{1/2}(1+b^2E)^{1/2}} \int_{s = \frac{z+bE}{2^{1/2}(1+b^2E)^{1/2}}}^{\infty} e^{-s^2} ds \qquad (10)$$

The approximation given for J in eqns. (9) and (10) involve the well known error function which is widely tabulated and for which there are simple computer approximations.[1] Formulas (9) and (10) are shown in example 1 following to approximate well to the integral J.

Typical Applications of the Results

The above functions provide an analytical tool to evaluate the effect of inlet particule size distribution on collection efficiency at constant precipitator flow and field conditions. This treatment is intermediate between the simplified Deutsch equation based on a uniform particle size, eqn. (2), and a detailed systems analysis.[6] The use of these asymptotic relationships will be demonstrated in the numerical examples given below.

Example 1

Problem:

Compute the overall efficiency of the precipitator whose grade-efficiency curve is given in Fig. 2 operating on the inlet dust distribution shown in Fig. 1. Evaluate the particle size distribution of the uncollected material.

Solution:

By replotting Fig. 2 on semi-logarithmic coordinates as in Fig. 3 and determining the slope, one finds k = 0.46 reciprocal microns. From Fig. 1, $\bar{d}_p$ = 12 microns and σ = 2.8. Therefore, $a = k\bar{d}p = 5.52$, $b = \ln \sigma = 1.03$, and $C = a^{1/2}b = 2.42$. From Fig. 5, $Ab^2 = 1.42$ giving A = 1.34. From eqn. (8),

$$\eta = 1 - \frac{e^{\frac{-A^2b^2-A}{2}}}{(1+Ab^2)^{1/2}} = 1 - 0.0654 \doteq 93.4\%$$

(rounded down)

A refinement of these calculations including a computer solution of eqn. (7) gives an efficiency of 1-0.065436 compared to the above figure. An efficiency of 1-0.065370 is obtained by direct numerical integration of eqn. (5). Agreement of these results is excellent.

The particle size distribution in terms of the fraction lost below a given size can be found by considering the integral J with upper limit given by $z = \ln (d_p/\bar{d}_p)/b$. J can be approximated by eqns. (9) or (10) depending upon the value of z. To obtain the cumulative particle size distribution, J must be divided by I, the infinite integral. The results of these calculations, set forth in Table 2, show quite good agreement for this example.

In addition, the preceding calculations can be compared with a more commonly employed method. The inlet dust distribution is broken up into a finite number of narrow size ranges, the amount collected for each range is determined, and these values are summed to find the overall collection efficiency. An example of this procedure is given by Stairmand.[8, 10] The calculations are summarized in Table 3. The overall collection efficiency is again 93.4%. The distribution of escaping material is slightly finer than the distribution obtained by direct numerical integration of the function J, shown previously in Table 2. The "exact" numerical integration distribution, with $\bar{d}_p$ of 2.7 microns and σ of 1.9, lies between this approximate distribution and the one obtained using the asymptotic expressions.

For this illustrative calculation, entries in Table 3 corresponding to the inlet particle size and collection efficiency have been computed from the appropriate functional forms rather than graphically as might normally be done for a routine calculation. The differences in efficiency and distribution are therefore caused only from taking a series of finite intervals in which the collection efficiency is assumed to be constant at its midpoint value.

In this example, the asymptotic analytical expressions derived in this paper have been shown to produce an overall efficiency equivalent to that obtained from direct numerical integration and a commonly employed approximate technique. In addition, the particle size distributions of all three methods are roughly comparable, with differences of the order of a few percent. The asymptotic functions are especially attractive for hand calculations when only the overall efficiency is desired. When a complete particle size distribution is required, the calculations involving eqns. (9) and (10) are more tedious than the method outlined by Stairmand, which would probably be used. When computer facilities are available, the asymptotic functions represent a savings in computer time over a standard numerical quadrature and are expected to require about the same order of magnitude of time as that used by the Stairmand type of calculation.

Example 2

Problem:

To increase collection efficiency, the precipitator of example 1 is to be doubled in size by increasing the length of its plates in the direction of gas flow. Calculate the new efficiency accounting for particle size distribution and by using the simplified Deutsch equation.

Solution:

To account for a change in plate length, one must vary k which is directly proportional to this dimension. In example 1, the parameters of the inlet dust and k = 0.46 led to an efficiency of 93.4%. When the size is doubled, k becomes 0.96 and the computation proceeds in a similar manner, giving an efficiency of 97.9%.

This calculation can be compared to an entirely different technique. As is sometimes done, eqn. (2), the simplified Deutsch equation for a monodisperse particulate, can be employed and thereby circumvent the use of an integral and all the difficulties involved in its evaluation. In this procedure, the observed 93.4% efficiency can be used to fix the value of the argument of the exponential at 2.7. Doubling the plate length makes this parameter 5.4 and gives an efficiency of 99.5%. Although the two efficiencies, 97.9% and 99.5%, appear close, the loss rates differ significantly by a factor of 4.

The efficiency as a function of length is plotted in Fig. 6. The asymptotic expression gives the efficiency shown by the solid curve, while the simplified Deutsch equation produces the broken line. The two provide equivalent results only in the vicinity of 93.4% efficiency where the Deutsch equation exponent was fitted.

Thus, the Deutsch equation predicts a greater efficiency at a given increment in length or a shorter additional length required to achieve a given increase in efficiency. This is the same sort of behavior demonstrated

Solution:

To account for a change in plate length, one must vary k which is directly proportional to this dimension. In example 1, the parameters of the inlet dust and k = 0.46 led to an efficiency of 93.4%. When the size is doubled, k becomes 0.96 and the computation proceeds in a similar manner, giving an efficiency of 97.9%.

This calculation can be compared to an entirely different technique. As is sometimes done, eqn. (2), the simplified Deutsch equation for a monodisperse particulate, can be employed and thereby circumvent the use of an integral and all the difficulties involved in its evaluation. In this procedure, the observed 93.4% efficiency can be used to fix the value of the argument of the exponential at 2.7. Doubling the plate length makes this parameter 5.4 and gives an efficiency of 99.5%. Although the two efficiencies, 97.9% and 99.5%, appear close, the loss rates differ significantly by a factor of 4.

The efficiency as a function of length is plotted in Fig. 6. The asymptotic expression gives the efficiency shown by the solid curve, while the simplified Deutsch equation produces the broken line. The two provide equivalent results only in the vicinity of 93.4% efficiency where the Deutsch equation exponent was fitted.

Thus, the Deutsch equation predicts a greater efficiency at a given increment in length or a shorter additional length required to achieve a given increase in efficiency. This is the same sort of behavior demonstrated

TABLE 1

COMPARISON OF APPROXIMATE METHOD WITH NUMERICAL INTEGRATION

$$I = \frac{1}{\sqrt{2\pi}} \int_{-\infty}^{\infty} e^{\frac{-t^{1/2}}{2} - ae^{bt}} dt$$

a	σ=1, b=ln σ = 0		σ=1.1052, b=0.1		σ=2, b=0.6931		σ=3, b=1.0986		σ=10, b=2.3026		σ=22026, b=10	
	Approx.	Num. Int.	Approx.	Num. Int.	Approx.	Num. Int.	Approx.	Num. Int.	Approx.	Num. Int.	Approx.	Num. Int.
0	1.0000	1.0000	1.0000	1.0000	1.0000	1.0000	1.0000	1.0000	1.0000	1.0000	1.0000	1.0000
1	0.3679	0.3679	0.3679	0.3679	0.3757	0.3733	0.3892	0.3848	0.4230	0.4196	0.4359	0.4773
2	0.1353	0.1353	0.1367	0.1367	0.1847	0.1838	0.2278	0.2263	0.3173	0.3185	0.4009	0.4500
3	0.04979	0.04979	0.05126	0.05127	0.1036	0.1031	0.1526	0.1520	0.2618	0.2643	0.3818	0.4341
4	0.01832	0.01832	0.01941	0.01941	0.06302	0.06279	0.1099	0.1097	0.2259	0.2288	0.3690	0.4229
5	0.006738	0.006738	0.007416	0.007415	0.04061	0.04049	0.08301	0.08293	0.2001	0.2032	0.3593	0.4143
6	0.002479	0.002479	0.002859	0.002858	0.02732	0.02726	0.06484	0.06484	0.1804	0.1835	0.3515	0.4072
7	0.0009119	0.0009118	0.001111	0.001111	0.01902	0.01898	0.05195	0.05199	0.1648	0.1678	0.3451	0.4013
8	0.0003355	0.0003354	0.0004356	0.0004355	0.01361	0.01359	0.04247	0.04253	0.1520	0.1549	0.3397	0.3962
9	0.0001234	0.0001234	0.0001721	0.0001721	0.009962	0.009951	0.03528	0.03535	0.1412	0.1441	0.3349	0.3917
10	0.00004540	0.00004540	0.00006854	0.00006854	0.007436	0.007429	0.02971	0.02977	0.1321	0.1349	0.3307	0.3877
11	0.00001670	0.00001670	0.00002753	0.00002751	0.005645	0.005640	0.02530	0.02536	0.1241	0.1269	0.3269	0.3841
12	0.000006144	0.000006144	0.00001113	0.00001113	0.004347	0.004345	0.02176	0.02182	0.1172	0.1198	0.3236	0.3808
13	0.000002260	0.000002260	0.000004536	0.000004534	0.003391	0.003390	0.01887	0.01893	0.1111	0.1136	0.3205	0.3778
14	0.0000008315	0.0000008315	0.000001862	0.000001861	0.002676	0.002675	0.01649	0.01654	0.1056	0.1081	0.3176	0.3750

TABLE 2

COMPARISON OF APPROXIMATE AND NUMERICALLY INTEGRATED UNCOLLECTED PARTICLE SIZE DISTRIBUTIONS FOR EXAMPLE 1

d_p(microns)	$J_{(approx.)}$*	Cum. Wt.%	$J_{(numerical)}$	Cum. Wt.%
1	0.00557	8.5	0.00563	8.6
2	0.0209	32.0	0.0219	33.5
3	0.0347	53.1	0.0372	56.9
4	0.0471	72.0	0.0481	73.6
5	0.0537	82.1	0.0550	84.1
6	0.0579	88.5	0.0592	90.5
7	0.0607	92.8	0.0618	94.5
8	0.0624	95.4	0.0632	96.6
9	0.0635	97.1	0.0641	98.0
10	0.0642	98.2	0.0646	98.8
∞	0.065436	100.	0.065370	100.

*In this example, $d_p \cong 2.96$ corresponds to $z=t^*$ and is therefore where we switch from eqn. (9) to eqn. (10).

TABLE 3

CALCULATION OF OVERALL COLLECTION EFFICIENCY FOR EXAMPLE 1 USING METHOD OUTLINED BY STAIRMAND

Size of Grade (microns)	% in Grade at Inlet	Collection Efficiency at Mean Size (%)	Overall Collection (%)	Cum. Wt.% Collected	Cum. Wt.% Escaping
0-1	0.8	20.6	0.165	0.18	9.7
1-2	3.3	49.8	1.64	1.9	34.9
2-3	4.7	68.3	3.21	5.4	57.7
3-4	5.4	80.0	4.32	10.0	74.1
4-5	5.6	87.4	4.89	15.2	84.9
5-6	5.2	92.4	4.80	20.4	91.0
6-7	5.0	95.0	4.75	25.5	94.9
7-8	4.7	96.8	4.55	30.3	97.1
8-9	4.3	98.0	4.21	34.8	98.5
9-10	4.0	98.7	3.95	39.1	99.3
10-15	15.6	99.7	15.55	55.7	100
15-20	10.5	100	10.5	67.0	100
20+	30.9	100	30.9	100	100
	100		93.435		

Figure 1

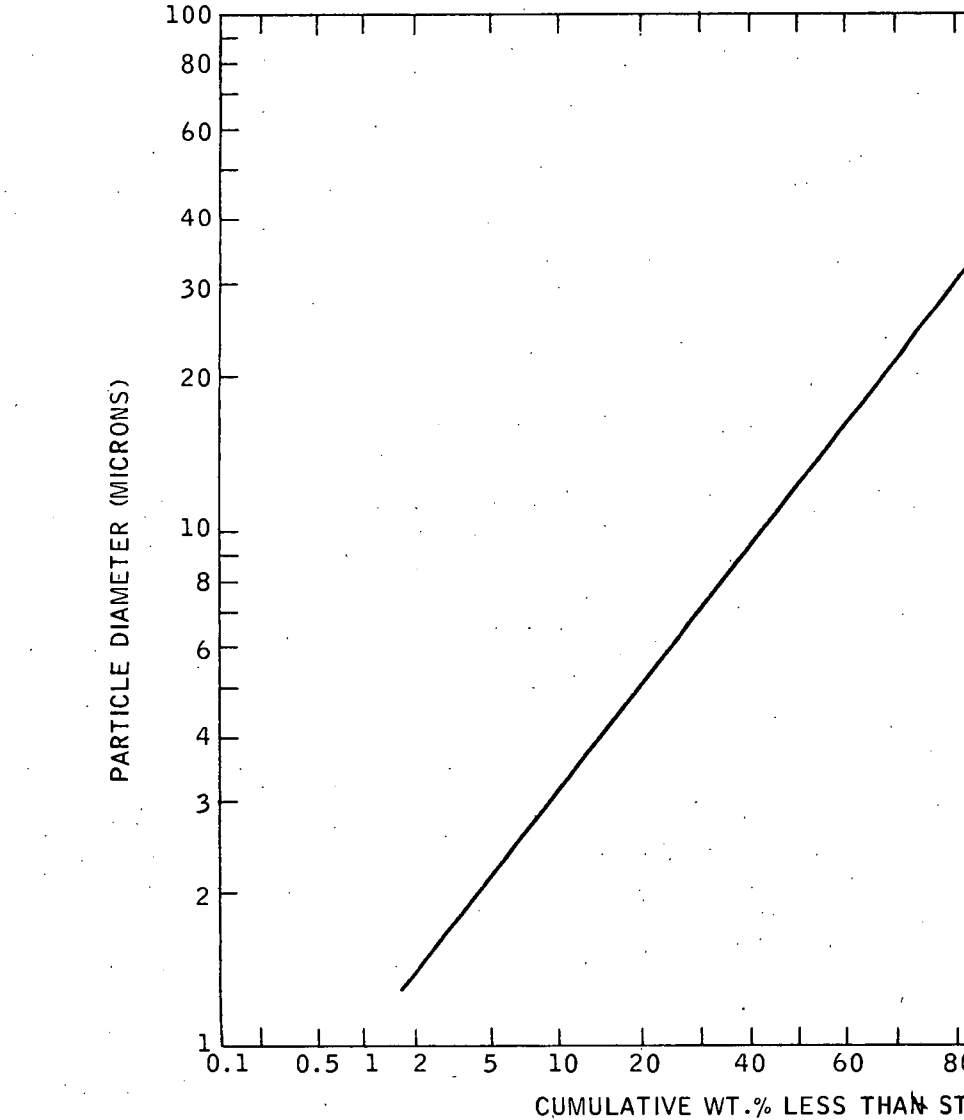
PARTICLE DIAMETER (MICRONS)
100
80
60
40
30
20
10
8
6
4
3
2
1
0.1
0.5
1
2
5
10
20
40
60
80
90
95
98
99.5
99.9
CUMULATIVE WT.% LESS THAN STATED SIZE

Figure 2

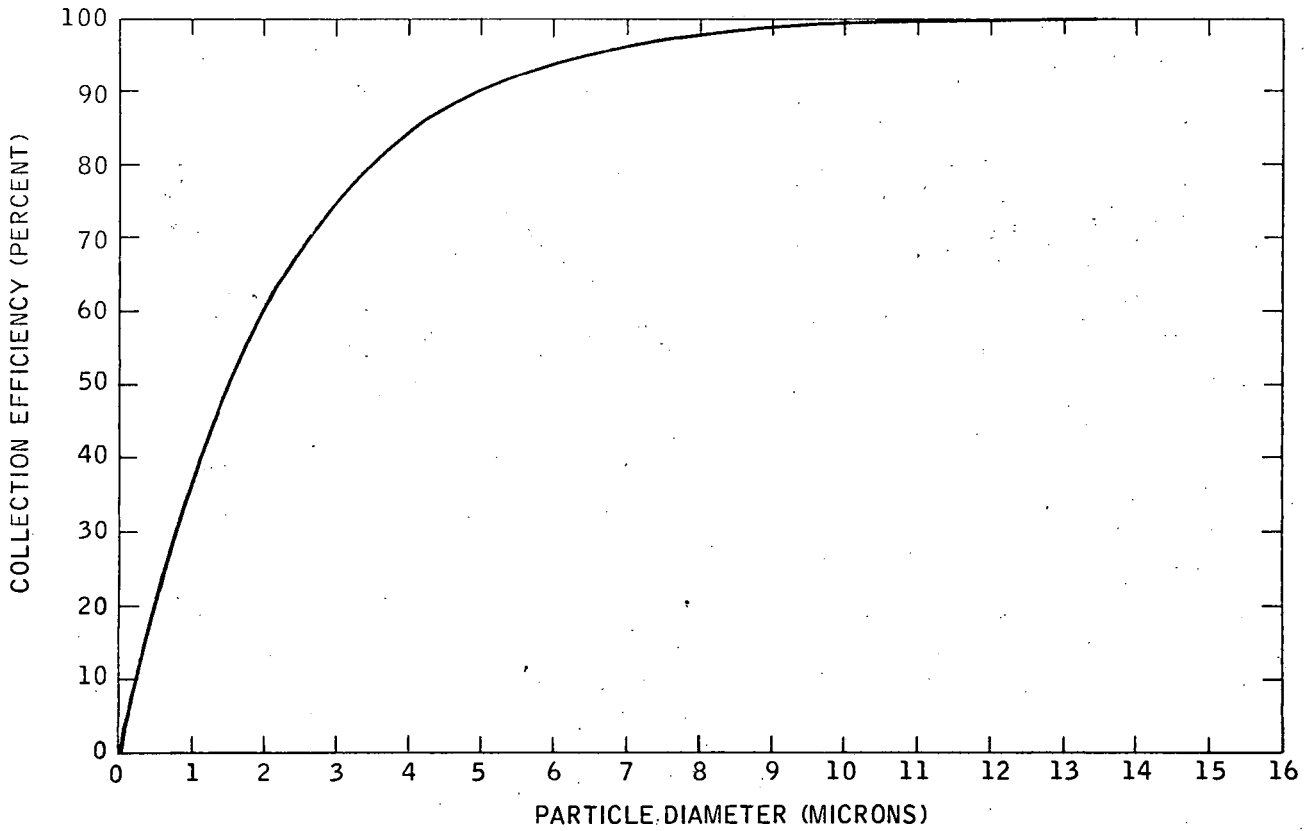
COLLECTION EFFICIENCY (PERCENT)
100
90
80
70
60
50
40
30
20
10
0
0
1
2
3
4
5
6
7
8
9
10
11
12
13
14
15
16
PARTICLE DIAMETER (MICRONS)

Figure 3

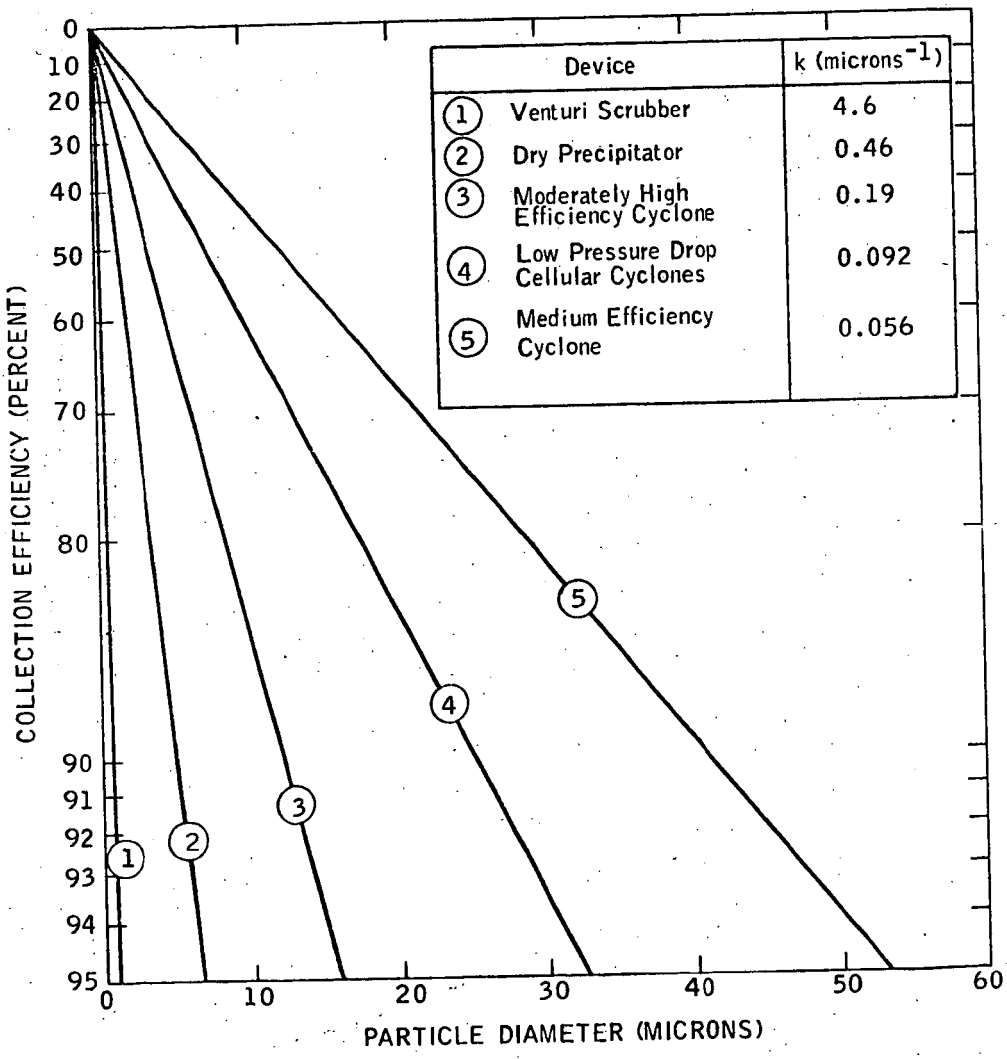
Device
k (microns^{-1})
1 Venturi Scrubber 4.6
2 Dry Precipitator 0.46
3 Moderately High Efficiency Cyclone 0.19
4 Low Pressure Drop Cellular Cyclones 0.092
5 Medium Efficiency Cyclone 0.056
COLLECTION EFFICIENCY (PERCENT)
0
10
20
30
40
50
60
70
80
90
91
92
93
94
95
PARTICLE DIAMETER (MICRONS)
0
10
20
30
40
50
60

Figure 4

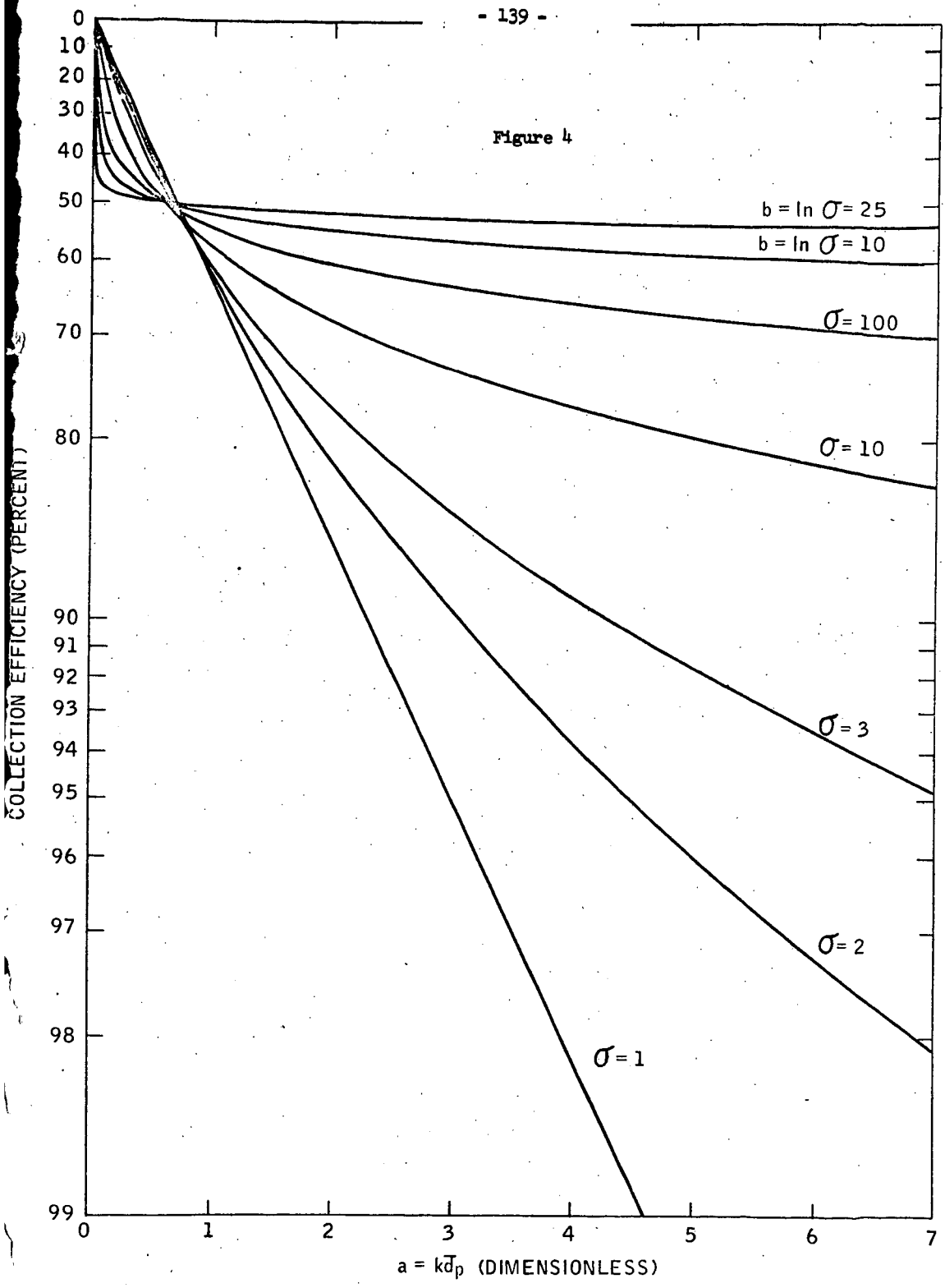
COLLECTION EFFICIENCY (PERCENT)
0
10
20
30
40
50
60
70
80
90
91
92
93
94
95
96
97
98
99
b = ln σ = 25
b = ln σ = 10
σ = 100
σ = 10
σ = 3
σ = 2
σ = 1
0
1
2
3
4
5
6
7
a = kd̄p (DIMENSIONLESS)

Figure 5

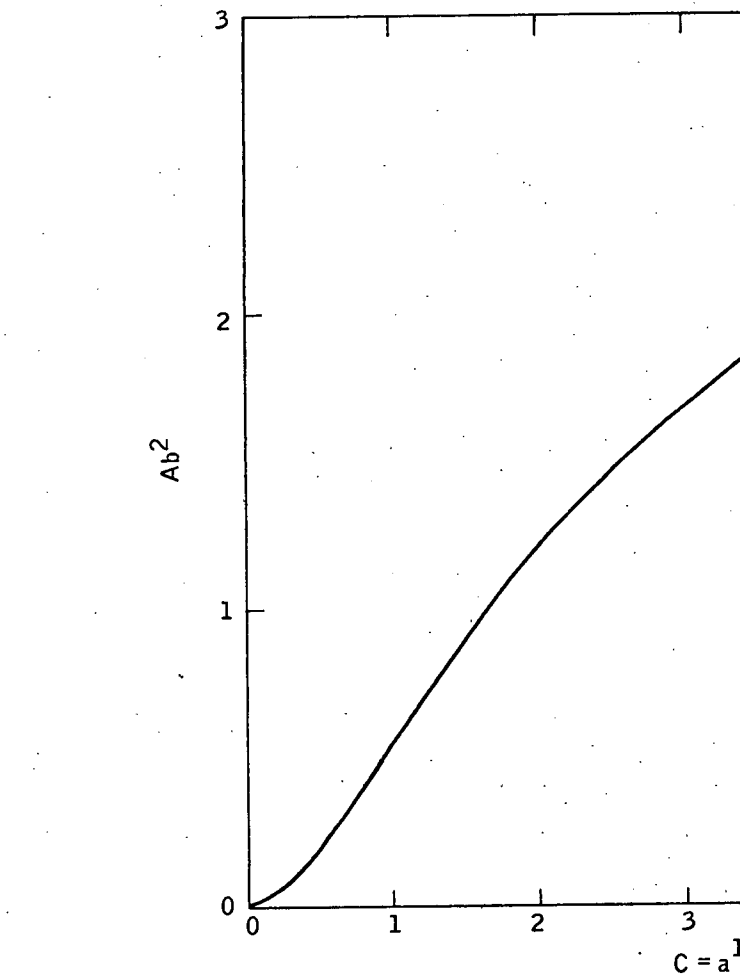

Figure 6

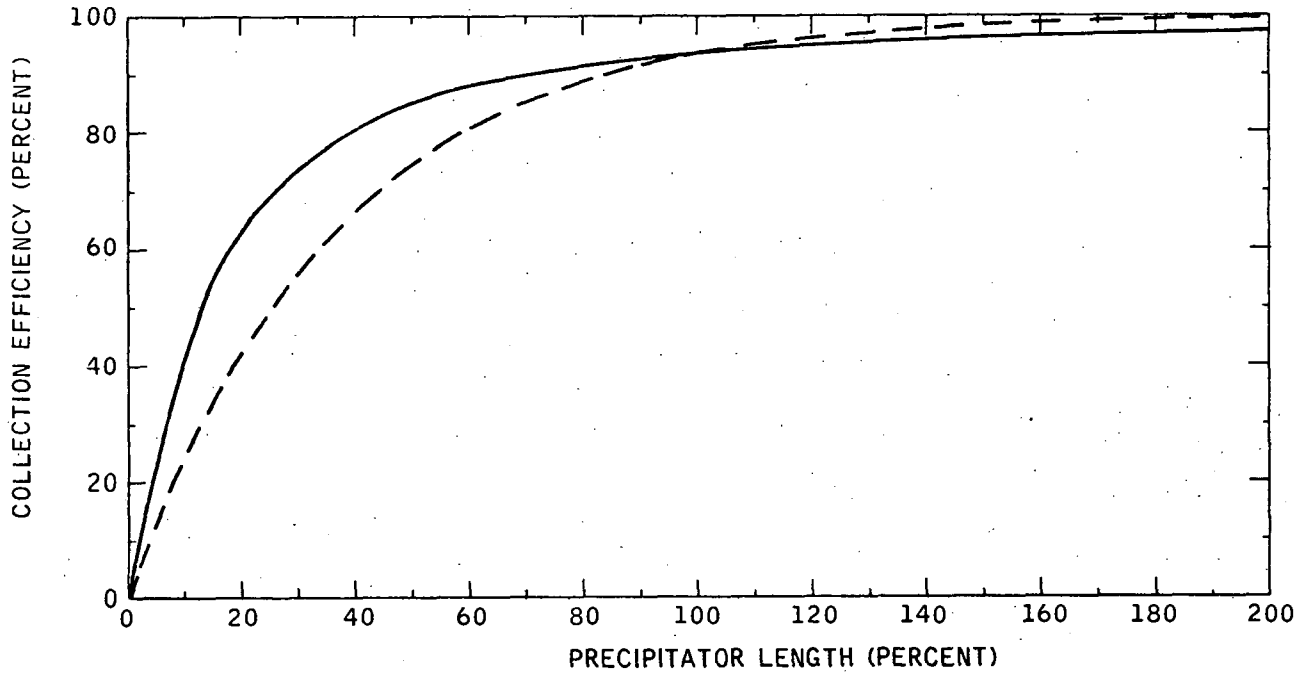
COLLECTION EFFICIENCY (PERCENT)
100
80
60
40
20
0
0
20
40
60
80
100
120
140
160
180
200
PRECIPITATOR LENGTH (PERCENT)

Notation

$a = k\bar{d}_p$

$A = ae^{bt*} = -Cu*/b^2 = -t*/b$

A_p = area of collection plates

$b = \ln \sigma$

$C = a^{1/2}b$

d_p = particle diameter

$\bar{d}_p$ = mass median diameter

e = base of natural logarithms

$E = ae^{bz}$

E_o = charging electrical field intensity

E_p = collection electrical field intensity

I = infinite integral in eqn. (5)

J = integral I with variable upper limit

k = collection parameter

Q = gas volumetric flow

s = variable of integration

t = variable of integration

t* = location of maximum point

$u* = t*/a^{1/2}$

w = effective migration velocity

z = variable upper limit of integral J = $\ln(dp/\bar{d}_p)/b$

Greek Letters

η = collection efficiency

μ = gas viscosity

π = numerical constant

σ = geometric standard deviation

LITERATURE CITED

1. Abramowitz, M. and Stegun, I. A., "Handbook of Mathematical Functions," NBS AMS 55, U. S. Government Printing Office, Washington, D. C. (1964).

2. Erdeleyi, A., "Asymptotic Expansions," Dover, New York (1956).

3. Finney, J. A., Jr., Power Eng., 72 (12), 26 (1968).

4. Henrici, P., "Elements of Numerical Analysis," Wiley, New York (1964).

5. Irani, R. R. and Callis, C. F., "Particle Size: Measurement, Interpretation, and Application," Wiley, New York (1963).

6. Nichols, G. B. and Oglesby, S. Jr., Paper presented at the 63rd Annual Meeting A.I.Ch.E., Symposium on Particulate Control Device Measurement, Paper 4a (1970).

7. Penney, G. W., J. Air Pollut. Contr. Ass., 19, 596 (1969).

8. Stairmand, C. J., J. Inst. Fuel (London), 29, 58 (1956).

9. _____, The Chemical Engineer (London), 194, CE310 (1965).

10. _____, Filtration & Separation, 7(1), 53 (1970).

11. White, H. J., Ind. Eng. Chem., 47, 932 (1955).

12. _____, "Industrial Electrostatic Precipitation," Addison-Wesley, Reading, Mass. (1963).

Appendix I

The solution of $u^* + Ce^{Cu^*} = 0$.

This equation is easily solved numerically by means of a suitable interation method if appropriate starting values are used. Suitable procedures include the Newton method or the ordinary iteration method accelerated by means of the δ^2 process.[4] The latter method was used to obtain the numerical values shown in Fig. 5 and Table A-1. Asymptotic solutions of the equation were used to yield reasonable starting values. The two asymptotic solutions for $-Cu^* \equiv Ab^2$ are

$$G_1(C) = \frac{2C^2\ (1+C^2)}{2(1+C^2)^2-C^4} \qquad (C \to 0) \qquad \text{(A1-1)}$$

and

$$G_2(C) = 2\ell n\ C - \ell n(2\ell n\ C) \qquad (C \to \infty) \qquad \text{(A1-2)}$$

These two asymptotes are compared with the numerical values in Table A-1. Since the $C \to \infty$ solution, eqn. (A1-2) involves a logarithmic scale, it only becomes accurate at extremely large (and impractical) values of C. However, it was observed that the difference between the numerical values and eqn. (A1-2) is nearly constant for $C \geq 2.5$, and thus in the table values of $G_2(C)+0.3$ are seen to yield accurate results for $C \geq 2.5$.

The asymptotic solutions given above are very useful in the asymptotic analysis of the integral I. Eqns. (A1-1) and (A1-2) show the asymptotic behavior of the quantity A with respect to a and b. For a or $b \to 0$, $A \to a$ and for $a \to \infty$, $A \to 2\ \dfrac{\ell n(a^{1/2}b)}{b^2}$.

TABLE A-1

COMPARISON OF NUMERICAL AND ASYMPTOTIC SOLUTIONS OF EQN. (7)

	Numerical	Asymptotic		
C	$-Cu^* = Ab^2$	$G_1(C)$	$G_2(C)$	$G_2(C) + 0.3$
0	0	0		
0.1	0.0099	0.0099		
0.3	0.0828	0.0828		
0.5	0.2039	0.2040		
1	0.5671	0.5614		
2	1.202	1.176	1.060	1.360
2.5	1.456	1.372	1.227	1.527
3	1.679	1.513	1.410	1.710
4	2.053		1.753	2.053
5	2.360		2.050	2.350
6	2.620		2.307	2.607
8	3.045		2.734	3.034
10	3.386		3.078	3.378
20	4.490		4.201	4.501
1000	11.38		11.19	11.49
10,000	15.67		15.51	

$$G_1(C) = \frac{2C^2(1+C^2)}{2(1+C^2)^2 - C^4}, \quad G_2(C) = 2\ln C - \ln(2\ln C)$$

Appendix II

Evaluation of $\frac{1}{(2\pi)^{1/2}} \int_{-\infty}^{\infty} e^{\frac{-t^2}{2} - ae^{bt}} dt \equiv I$

We proceed by splitting the integral by means of $\int_{-\infty}^{\infty} = \int_{-\infty}^{t*} + \int_{t*}^{\infty}$ where $t*$ is the solution of eqn. (6). Thus $I = I_1 + I_2$ where $I_1 = \int_{-\infty}^{t*}$ and $I_2 = \int_{t*}^{\infty}$. First consider I_2, which turns out to be much easier to analyze than I_1. (It happens that to the first approximation, I_1 and I_2 are equal). By translating the origin of coordinates to $t*$ through $t-t* = u$, we get

$$I_2 = \frac{e^{\frac{-b^2A^2}{2}}}{(2\pi)^{1/2}} \int_{u=o}^{\infty} e^{\frac{u^2}{2} + Abu - Ae^{bu}} du \qquad \text{(A2-1)}$$

Since the new integrand, by way of its construction, is a maximum near u=0, it is natural to approximate to the integrand in this vicinity in hopes that though the approximation may not be good in other regions, these regions contribute only a small part to the integral. The best procedure seems to be the following. Write

$$e^{bu} = 1 + bu + \frac{b^2u^2}{2} + e^{bu} - 1 - bu - \frac{b^2u^2}{2}.$$

Then expand the exponential in eqn. (A2-1) to get

$$I_1 = \frac{e^{\frac{-b^2A^2}{2} - A}}{(2\pi)^{1/2}} \int_{u=o}^{\infty} e^{-(1+b^2A)\frac{u^2}{2}} \left[1 - A(e^{bu} - 1 - bu - \frac{b^2u^2}{2})..\right] du \qquad \text{(A2-2)}$$

where the error incurred by taking 1 for the quantity in square brackets is negative and less in magnitude than the next term.

By performing the integration we get

$$I_2 = \frac{e^{\frac{-b^2A^2}{2} - A}}{(2\pi)^{1/2}} \left[\frac{\pi^{1/2}}{(2g)^{1/2}} - A\left\{ \left(\frac{2}{g}\right)^{1/2} e^{\frac{b^2}{2g}} \int_{s=\frac{-b}{(2g)^{1/2}}}^{\infty} e^{-s^2} ds - \left(\frac{\pi}{2g}\right)^{1/2} - \frac{b}{g} - \frac{b^2\pi^{1/2}}{(2g)^{3/2}} \right\} \right] \tag{A2-3}$$

where $g \equiv (1 + b^2A)$

The error made by approximating the quantity in square brackets by the first term is negative and less in magnitude than the next term. It is easily shown eqn. (A2-3) that the relative error associated with using just the first term in square brackets goes to zero for either $a \to 0$, $a \to \infty$ or $b \to 0$. The integral I is transformed by means of $t^* - t = s$ and becomes

$$I_1 = \frac{e^{\frac{-b^2A^2}{2} - A}}{(2\pi)^{1/2}} \int_{s=o}^{\infty} e^{\frac{-s^2}{2} - Abs - Ae^{-bs}} ds \tag{A2-4}$$

Here again the integrand is approximated near its maximum (s=0) and to a first approximation for either $a \to 0$, $a \to \infty$ or $b \to 0$

$$I_1 \to \frac{e^{\frac{-b^2A^2}{2} - A}}{2g^{1/2}}$$

However, in the case of I_1, the demonstration of the validity of this result is much more involved than it was in the case of I_2 and the lengthy details are omitted.

Appendix III

Other Asymptotic Expansions to $I = \frac{1}{(2\pi)^{1/2}} \int_{-\infty}^{\infty} e^{\frac{-t^2}{2} - ae^{bt}} dt$

For $b \to \infty$, $I \to 1/2$ in accordance with

$$I = 1/2 + R_1, \quad |R_1| \leq \frac{1}{\sqrt{2\pi}} \max \left[\frac{a}{b}, \frac{e^{-a}}{ab}\right] \tag{A3-1}$$

Note the curve for b=25 of Fig. 4 is approaching this limit.

For $b \to 0$ we have

$$I = e^{\frac{-A^2b^2}{2}} \left[1 - A\left(e^{\frac{b^2}{2}} - 1\right) ..\right] \tag{A3-2}$$

Eqn. (A3-2) is useful since it has the property that the error made by taking the term in square brackets equal to 1 is negative and less in magnitude than $A\left(e^{\frac{b^2}{2}} - 1\right)$.

For $a \to 0$

$$I \sim \sum_{i=0}^{\infty} \frac{(-1)^i a^i e^{\frac{b^2 i^2}{2}}}{i!} = 1 - ae^{\frac{b^2}{2}} + \frac{a^2 e^{2b^2}}{2!} - \frac{a^3 e^{\frac{9b^2}{2}}}{3!} .. \tag{A3-3}$$

This series diverges for any $b > 0$, but it is asymptotic in the sense that the error is of the same sign as the first neglected term and less than it in magnitude. Therefore, the series is of use computationally for sufficiently small values of a.

Appendix IV

Evaluation of $\frac{1}{(2\pi)^{1/2}} \int_{-\infty}^{z} e^{\frac{-t^2}{2} - ae^{bt}} dt = J$

It is convenient to consider separately the cases $z < t^*$ and $z > t^*$. For $z < t^*$, the maximum of the integrand is at z and accordingly we move the origin of coordinates to z and approximate to the integrand in this vicinity. Thus J becomes

$$J = \frac{e^{\frac{-z^2}{2}}}{(2\pi)^{1/2}} \int_{\omega=o}^{\infty} e^{z\omega - \frac{\omega^2}{2} - /Ee^{-b\omega}} d\omega \qquad \text{(A4-1)}$$

where $E \equiv ae^{bz}$

By approximating the exponential near $\omega = 0$, we get

$$J \doteq \frac{e^{\frac{-z^2}{2} - E}}{(\pi)^{1/2}(1+b^2E)^{1/2}} e^{\frac{(bE+z)^2}{2(1+b^2E)}} \int_{s=\frac{(bE+z)}{2^{1/2}(1+b^2E)^{1/2}}}^{\infty} e^{-s^2} ds \qquad (z \leq t^*) \quad \text{(A4-2)}$$

The integral appearing in eqn. (A4-2) is just the complementary error function which is widely tabulated and for which there are simple computer approximations.

For $z > t^*$, it is convenient to calculate J by means of $K = \int_{-\infty}^{\infty} - \int_{z}^{\infty}$.
Then an approximation of the type discussed in the previous paragraph gives

$$J \doteq I - \frac{e^{\frac{-z^2}{2} - E}}{\pi^{1/2}(1+b^2E)^{1/2}} e^{\frac{(bE+z)^2}{2(1+b^2E)}} \int_{s=\frac{bE+z}{2^{1/2}(1+b^2E)^{1/2}}}^{\infty} e^{-s^2} ds \qquad (z>t^*) \qquad \text{(A4-3)}$$

Note that for $z = t^*$ the sum of the approximations to $\int_{-\infty}^{z}$ and $\int_{z}^{\infty}$ just adds up to the approximation given for $\int_{-\infty}^{\infty}$.

A STUDY OF FLY ASH REACTIONS AND DEPOSIT FORMATION IN A LARGE, CYCLONE-FIRED STEAM GENERATOR

A. A. Orning

U. S. Department of the Interior, Bureau of Mines,
Pittsburgh Energy Research Center, Pittsburgh, Pa.

Introduction

Many, if not most, of the problems peculiar to the use of coal as a fuel are related to its mineral matter content. The ash and slag products cause fouling and sometimes corrosion of heat transfer surfaces, are hard to remove when slag deposits become massive, are difficult to contain when the slag is fluid, and are costly to remove as particulate matter in the stack gases. The purpose of this paper is to discuss the release of mineral matter in burning coal and to present data on reactions of ash deposits with combustion product gases in a large cyclone-fired steam generator. Conclusions will be drawn that must be interpreted as pertinent to the particular unit though based in part on observations in other units. The intent is to demonstrate that valuable information can be gained by systematic sampling and analysis of fly ash and ash deposits.

The Release of Mineral Matter

Ash, as formed from the mineral matter of coal in the ASTM Standard Method,[1/] has analyses as illustrated by samples 8 and 9 of Table I for two Illinois coals. Several things are noteworthy: 1) Carbonates are converted to oxides, 2) sulfur is retained as sulfate to the extent that sulfate formation precedes carbonate decomposition, and 3) the weight percentages of ash components, represented as oxides, add approximately to 100%. When the ash is formed under high-temperature conditions, as in the steam generator furnace rather than the temperature-controlled muffle furnace used for the ash determination, a lesser proportion of the sulfur is retained as sulfates and the alkali metals are at least partially volatilized. Vapor pressures for various alkali materials are given in Table II. The free alkali metals are most volatile, but equilibria favor conversion to the hydroxides. The oxides should be considered, although equilibria also favor their conversion to the hydroxides. Little information is available on the kinetics of such high-temperature, gas-phase reactions. Acid-base reactions are fast in water solution but may be slow in the gas phase. HCl gas seems relatively inert. Alkaline mists have been observed to fall out of the plume from incineration of organic wastes with high NaCl content. These considerations suggest that the hydroxides are the probable mode of transport of alkali metals in the hot combustion gases.

TABLE I.- Analyses of ash and slag samples, weight percent

No.	Location	SO_3	Fe_2O_3	Al_2O_3	SiO_2	CaO	MgO	Na_2O	K_2O	Total
1	Slag tank	0.25	19.7	17.6	45.8	8.67	0.95	2.16	1.99	97.1
3	Reheat superheater	10.2	21.0	16.4	32.5	10.95	.80	2.80	2.19	96.8
4	Primary superheater	2.2	18.6	18.3	47.1	5.96	.86	2.47	2.04	97.5
5	Economizer hopper	5.0	20.6	17.4	43.2	5.79	.75	2.56	2.13	97.4
6	Air heater hopper	2.2	21.7	17.6	45.4	7.61	.86	2.12	2.05	99.5
7	Precipitator hopper	3.5	18.9	17.6	45.8	5.04	.90	2.91	2.82	97.5
8	Coal ash, A	7.5	28.2	15.5	35.7	7.68	.78	2.43	1.83	99.6
9	Coal ash, B	8.0	17.2	18.9	44.5	7.55	.91	1.98	1.83	100.9

TABLE II. - Temperatures at selected vapor pressures

Component	T °C 1 mm	10 mm	100 mm
Na	439	549	701
K	341	443	586
NaOH	739	897	1111
KOH	719	863	1064
NaCl	865	1017	1220
KCl	821	968	1164

Iron sulfide, FeS, and metallic iron tend to appear with deficient air supply. This is aggravated in wet bottom furnaces when pyrite (FeS_2) impinges on the slag surface. The iron in coal is present primarily as pyrite. Bailey and Ely[2] have shown that iron tends to segregate into slag and into furnace deposits. The author has observed a furnace with front wall burners and a plan area too small to prevent flame impingement on the wall surfaces. Iron content of the wall slag was over three times that expected from the coal ash analysis. It appeared that oxygen was deficient in the area of flame impingement and that liquid droplets of FeS were preferentially adhering to the wall, although intermittent oxidation gave an oxidized slag.

Fireside corrosion associated with segregated deposits high in alkali-iron sulfates were first found on furnace wall tubes of wet bottom furnaces.[3,4] Presence of CO in the local gas stream was indicative of local oxygen deficiency and flame impingement with preferential adherence of FeS droplets and high local heat transfer rates. However, the segregated deposits were found to be sulfates with detectable sulfide only at the interface between the deposit and the tube metal. Intermittent oxidizing conditions convert sulfides to sulfates. With tube surface temperatures on the order of 400 °C, the complex alkali-iron pyrosulfates become stable liquids. While these liquids in part may be corrosion products, they in turn are cause for electrolytic corrosion if not the active corrosive agents.

Reactions between sulfur oxides and fly ash have been the subject of study and speculation for many years. Johnstone[5] concluded that fly ash from stoker-fired boilers had a little catalytic action on the oxidation of sulfur dioxide in flue gas. Crossley, Poll and Sweett[6] studied these reactions to explain findings of the Boiler Availability Committee that firing of pulverized coal over the back end of mechanical stokers was effective in controlling acidic deposits in the boiler. The appearance of the typical alkali-iron-aluminum sulfates on superheater tubes brought renewed interest in the reactions between fly ash and combustion gases. The extensive literature has been reviewed by Reid.[7] The deposits are characterized by water solubility, a low pH, high content of alkali, iron, aluminum and sulfate, and relatively low contamination by other constituents of fly ash. These deposits underlie typical ash deposits. They have an amorphous or microcrystalline appearance when cold but sometimes show signs of having been liquid. They appear where gas temperatures, the thickness of the overlying ash deposit, and the steam conditions are such that the resulting heat transfer produces temperatures near the tube surface approaching 650 °C. The segregated deposit may be separated from the tube metal by a poorly consolidated oxide scale. The author has also found samples where liquid wetted the metal tube and penetrated under the oxide scale so as to bend it away from the tube surface. Relatively low occlusion of fly ash in the segregated deposit indicates that components not soluble in the deposit are mechanically ejected by cyclic melting and solidification. The resulting deposit, from American bituminous coals, has a somewhat variable composition, particularly the

proportion of iron and aluminum sulfates, but is so characteristically different from the overlying fly ash deposits that it is visually detectable without need for chemical analysis.

Occurrence of the segregated deposit under typical ash deposits has caused speculation as to whether the deposit was formed first and the fly ash deposited later or whether the segregated material was synthesized beneath the fly ash deposit.

Synthesis of the complex sulfates requires a partial pressure of SO_3 higher than that found in the main stream of combustion gases. Anderson and Goddard[8] conclude that the SO_2-SO_3 reaction reaches equilibrium within the deposit and that solution phenomena at operating temperatures reduce the necessary partial pressure of SO_3 below that exhibited by pure phases of alkali-iron and alkali-aluminum sulfates that appear in the deposit after cooling.

While information on reactions between sulfur oxides and fly ash is sketchy, there is even less information on reactions involving the alkali metals. Weintraub, Goldberg and Orning[9] found that the alkali content of fly ash, subjected to a temperature gradient in a flue gas atmosphere, migrated towards a cold surface at 375°C. The complex alkali sulfates did not appear. In the absence of a supply, beyond that of the original fly ash, there was insufficient alkali for the synthesis. Since the alkali components of the mineral matter of coal are volatile under combustion conditions, it seemed desirable to gather data on the reabsorption of alkali by fly ash and by deposits at various points within a coal-fired steam generator. A study of deposits in a cyclone-fired unit seemed preferable because the high temperatures within the cyclone would assure more complete volatilization of the alkali components.

The Steam Generator

The steam generator cross section is shown in Fig. 1. It was rated at 3,290,000 lb of steam/hr, 3625 psig and 1005°F superheat with 575 psig and 1005°F reheat. It had 10 cyclones, 10 ft in diameter, five each on the front and rear walls. Sampling points are shown by the circled numerals, except for the electrostatic precipitator hopper which is not shown. The furnace wall tubes were fully studded to a level about 5 ft below the gas recirculation ports. A thin, glassy slag coat was intact throughout the studded zone following shutdown. Slag shedding had occurred on all upper wall surfaces except in the corners just above the studding and on the walls under some of the gas recirculation ports.

Ash and Slag Samples

Two southern Illinois bituminous coals were used. Analyses of the ash and slag samples are shown in Table I. Data on the mole percent basis, shown in Table III, are more revealing. Unfortunately, the two coals that were used have somewhat different ash analyses. The SO_3 is equivalent to about 70% of the CaO for both coal ashes, while sulfur in ash accounted for 24.6% of the sulfur in coal A and 38.5% of the sulfur in coal B. Retention of sulfur in the coal ash, as produced at 700° to 750°C by the standard method for ash content, is related to the calcite content rather than to the sulfur content of the coal.

The composition of various slag, deposit, and fly-ash samples may be expected to depend upon opportunities for segregation, on temperatures at various points along the gas flow path, and on the readsorption of sulfur and alkali components. The temperatures were not measured but were probably on the order of over 1700°C in the cyclone, 1000°C in the secondary superheater, location 2, and 325°C at the air heater, location 6.

TABLE III.- Ash analyses, mole percent, and physical characteristics

No.	Location	Color[a]	Mag.[b]	SO_3	Fe_2O_3	Al_2O_3	SiO_2	CaO	MgO	Na_2O	K_2O
1	Slag tank	BL.	1	0.2	9.5	13.3	59.0	11.9	1.8	2.7	1.6
6	Air heater	BL.	3	2.1	10.4	13.2	58.0	10.4	1.6	2.6	1.7
4	Primary superheater	R.B.	2	2.2	8.9	13.9	60.4	8.2	1.6	3.1	1.7
5	Economizer hopper	B.R.	2	4.9	10.2	13.4	56.7	8.2	1.5	3.3	1.8
3	Reheat superheater	B.R.	0	10.2	10.5	12.9	43.6	15.7	1.6	3.6	1.9
7	Precipitator hopper	G.B.	2	3.4	9.2	13.4	59.4	7.0	1.7	3.6	2.3
8	Coal ash, A	-	-	7.6	14.3	12.3	48.3	11.1	1.6	3.2	1.6
9	Coal ash, B	-	-	7.5	8.0	13.8	55.2	10.0	1.7	2.4	1.4

[a]Color code: BL., black; R.B., red-brown; G.B., gray-brown; B.R., brick-red.
[b]Scale of increasing magnetic character.

Sulfur content of the slag is almost immeasurably low. The 0.2 mole of SO_3 corresponds to 0.1 wt percent of sulfur, which is reported to the nearest 0.1%. The sodium and potassium contents of the slag are comparable to those of the coal ashes. Slag from the cyclones flows across the furnace floor to the slag drip. Either the alkali metals were not substantially volatilized in the cyclones or they were readsorbed as the slag flowed across the furnace floor.

Deposit samples were not taken from location 2, Fig. 1 (lead tube of the last platen of the secondary superheater). Visually identifiable complex alkali-iron-aluminum sulfate, covered by a thin shell of ash, was found on these tubes. The ash shell had partially shed on cooling of the furnace. Large sections could be removed intact with light finger pressure on the edge to expose the underlying sulfate deposit. The shell was so thin that clean separation from the underlying sulfate deposit could not be assured for the purpose of chemical analysis.

Deposits at location 3 (lead tube of the reheat superheater platen) were shaped like antlers jutting into the gas stream and were joined by a thin shell across the front of the tube. They were so hard that the author could not break them off by hand though they projected about 3 inches in front of the tube. The analysis gave an exceptionally high content of SO_3 and maximum values for the alkali metals, except K_2O in the precipitator hopper sample. The surface of the deposit was dusty, and fracture surfaces showed no indication of fusion, suggesting that the ash was cemented by formation of alkali sulfates within pores of the deposit.

The samples from location 4 (the top of the primary superheater) were hard nodules blown from an unknown location and too large to pass between the superheater tubes. While these nodules were as hard as sample No. 3, the sulfur content was not as high. The underlying tubes were free of deposits.

The economizer hopper (location 5) was located below the downflow section of convective heat transfer tubes. The air heater hopper was under the flow reversal duct between sections of the air heater. The classifying action of changes in flow direction, compared to electrostatic precipitation, may be responsible for the differences in analysis between samples from the economizer hopper, the air heater hopper, and the precipitator hopper, locations 5, 6, and 7. There is also a progressive drop in temperature between these locations.

The sample analyses are remarkably consistent except for the variation in SO_3 content and a disproportionation between lime and silica in sample No. 3. The iron content of the hopper and deposit samples is between those of the two coal ashes, while the silica contents, with the one exception, are higher than that of either coal ash.

The hopper and deposit samples showed remarkable differences in color and magnetic properties. Table III gives data from gross appearance. Microscopic examination showed heterogeneous character. The slag tank sample looked like pulverized black glass with a few translucent wedges and a few magnetic particles, presumably magnetite. The brick-red material from the reheat superheater tube had a very small number of magnetite particles. The economizer hopper and superheater nodule samples had increasing proportions of magnetite mixed with the brick red. The air heater sample appeared almost as black as the slag tap sample, and had a large portion of magnetite with a sprinkling of small red particles on the surface of the larger black particles. The precipitator hopper sample had a considerable portion of magnetite with enough whites (some opalescent beads) and reds to give a gray-brown appearance. Almost all black particles, except those from the slag tank, were magnetic, presumably magnetite. The analyses for iron are given in terms of Fe_2O_3 without regard to the actual state of oxidation. The brick red color is due to ferric oxide, and the color variations may be used to infer variations in ferric oxide content.

Discussion

Most of the ash from cyclone combustion is collected in the slag tank with almost negligible sulfur content. Deposits with high sulfur content are formed over long periods of time and represent a negligible part of the material balance. The fly ash has a significant sulfur content but represents a minor fraction of the mineral matter input. Most of the sulfur passes through the system as SO_2, but oxidation to SO_3 and sulfate formation by reaction with other mineral matter components have considerable effect on deposit formation.

The behavior of iron is of particular interest. It is present in the coal almost entirely as pyrite, often distributed as very fine particles. Rapid heating to 2200°C produces liquid droplets approximating FeS, ferrous sulfide.[10] The sequence of melting, decomposition, and oxidation is unknown. Larger particles are probably thrown onto the slag within the cyclone. Smaller particles are converted in suspension to finely divided ferric oxide. The author has observed a cyclone-fired unit with a mechanical but no electrostatic precipitator. The stack plume was brick red. Had it been black it would have been rated number 4 smoke. The finely divided ferric oxide produces a dust coating on tube surfaces. At appropriate temperature levels, oxidation of SO_2 to SO_3 within the dust layer and reaction with adsorbed alkali metals produces the complex alkali-iron sulfates. Depending upon temperatures and temperature gradients, these sulfates may act as cementing agents or may accumulate as a segregated phase near the tube surface. Cyclic melting and freezing then causes ejection of non-soluble particulates and accumulation of the segregated deposit.

A systematic variation in alkali metal content was not apparent until the data were arranged in the sequence of Table III. Data for the slag tank sample are listed first. Those for the precipitator hopper sample and the coal ashes are listed last. Intervening data are in the sequence of increasing content of ferric iron as inferred from color. Variation from the sequence of positions along the flow path is a result of segregation of particulate matter and the action of retractable blowers used periodically to blow loose deposits off tube surfaces. The highest content of ferric iron was found in the hard deposit on the reheat superheater tube. Dusty deposits are blown off the tubes by the retractable blowers.

Depending upon agglomeration, these tend to fall out in the economizer hopper or carry through to the electrostatic precipitator. Absorption of the alkali metals appears to be favored by the finely divided ferric oxide with some effect of temperature on opportunities for sulfate formation. Temperatures are lowest in the precipitator. Conditions are most favorable for reaction with SO_3 within deposits on the secondary superheater, location 2, and the reheat superheater, location 3. Material balances are obscured by differences between the coals and the unknown times required for deposit formation. High SO_3 content in segregated deposits is negligible in comparison to total flow over the time of their formation. Relatively high content in the precipitator sample is offset by the larger portion of the total ash collected in the slag tank. Immeasurably lower content in the slag tank sample is sufficient to provide material balance. The disproportionation of MgO and SiO_2, in the deposit at location No. 3, the reheat superheater lead tube, is explainable in terms of the results of intermittent operation of retractable blowers. Acid formation and alkali adsorption extend through the interface between the cemented deposit and the dusty outer coat. Basic constituents, as against the acidic silica present in segregated particles, are preferentially retained when the dust coating is intermittently removed by the blower action.

Recommendations for Future Study

Data presented here are for samples taken from a cyclone-combustion-fired unit. It has often been observed that these units produce reddish fly ash rather than the typical gray fly ash from pulverized-coal-fired systems, indicating the presence of finely divided ferric oxide. Nevertheless, the data indicate the possibilities for better understanding of the reactions involved in deposit formation. Supplemental data on temperatures, gas compositions, and particulate samples taken from the gas stream at various points along the gas flow path would be helpful. Preparation for taking samples from less accessible positions would also be helpful.

Laboratory studies of reactions between gases and mineral matter components become meaningful only when interpreted in relation to the conditions and materials that exist within actual steam generator systems. Laboratory studies should be encouraged, but they must be coordinated with actual conditions in large steam generators.

Conclusions

1) Samples of fly ash and deposits were obtained from various locations in a large, cyclone-fired steam generator.

2) Wide variations in color were due to variations in ferric oxide content.

3) Variations in alkali metal content were related qualitatively to variations in ferric oxide content and temperatures.

4) Typical segregated deposits of complex alkali-iron-alumina sulfates were visually identified within the secondary superheater.

5) A hard deposit on the reheater superheater probably was formed by the cementing action of sulfates formed within the pores of an overlying dusty deposit and incremental buildup of cemented material left after each cycle of retractable blower operation.

References

1/ ASTM Standard Method of Laboratory Sampling and Analysis of Coal and Coke, D271-64.
2/ Bailey, E.G., and Ely, F.G., Tr. Am. Soc. Mech. Engrs. 63, 465-71 (1941).
3/ Reid, W.T., Corey, R.C., and Cross, B.J., Tr. Am. Soc. Mech. Engrs. 67, 279-88 (1945).
4/ Corey, R.C., Cross, B.J., and Reid, W.T., Tr. Am. Soc. Mech. Engrs. 67, 289-302 (1945).
5/ Johnstone, H.F., Univ. of Illinois Eng. Exp. Sta. Bull. 228, 1931, pp. 44, 45.
6/ Crossley, H.E., Poll, A., Sweett, F., J. Inst. Fuel 21, 207-13 (Apr. 1948).
7/ Reid, W.T., External Corrosion and Deposits-Boilers and Gas Turbines, Elsevier, New York, 1971.
8/ Anderson, C.H., and Goddard, C.W., J. Inst. Fuel 61, 357-64 (1968).
9/ Weintraub, M., Goldberg, S.A., and Orning, A.A., Tr. Am. Soc. Mech. Eng., Series A, 83, 444-50 (Oct. 1961).
10/ Halstead, W.D., and Raask, E., J. Inst. Fuel 62, 344-49 (1969).

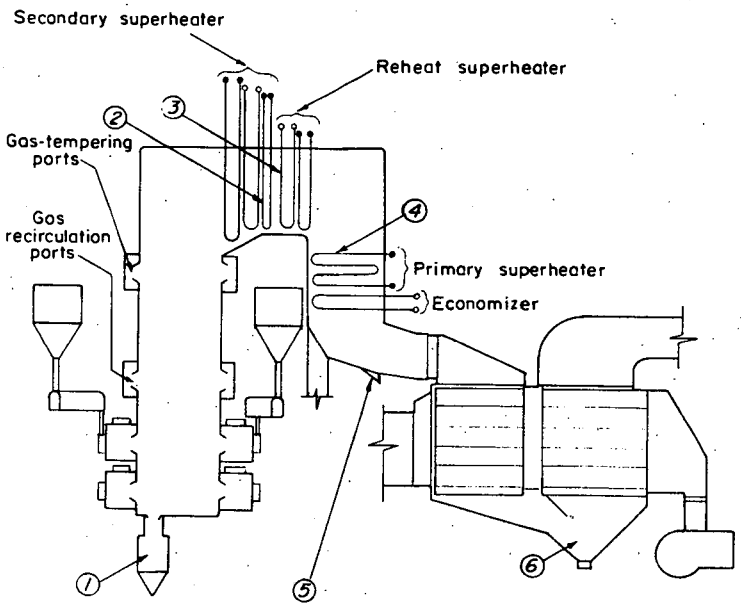

Figure 1.- Sampling locations in the cyclone fired steam generator. Location 7, the precipitator hopper is not shown.